Neuroradiology: History and New Research Technologies

1

1.1 Introduction

Neuroradiology is a part of general radiology that is dedicated to the diagnostic examination of the brain and spinal cord. The history of neuroradiology, as a whole, reflects the history of radiology development. The birthday of radiology could be considered as 8 November 1895; it was on this day that W. K. Roentgen was experimenting with a cathode tube and discovered a new type of radiation (emission) with high penetrating capacity. Eventually he named this new type of radiation the "X-ray".

Roentgen made the first X-ray image—a skull—in December 1895. In the beginning of January 1896, after 2 months of painstaking research, he published the article "On a New Kind of Rays", and on 23 January he made a presentation on his discovery to a session of the Würzburg Physics–Medical Society. He showed images of bony skeleton structures, created by X-rays passed through a human body to the surface of the photographic plate.

Roentgen's discovery gave powerful impetus to research in physics, and the world's scientific community of physicists, mathematicians, biologists and physicians welcomed this breakthrough. For his discovery of X-rays, he received the first Nobel Prize in physics in 1901. X-rays promptly became the new tool in physics research, and in medicine, they provided many opportunities to visualise the internal structures of the human body. Commonly, X-rays were named "Roentgen rays", the cathode tubes "Roentgen tubes" and the machines for obtaining the images of the internal structure "Roentgen machines".

The first diagnostic machine was revealed in Germany on 26 January 1896. It could capture the image of bone structures, formed on the photographic layer of specially prepared plate by passing X-rays through the body. For more than a century, medicine has been able to visualise internal organs and bones via X-rays. This method is known as *radiography*. The successful application of X-rays for visualisation of high-contrast bone structures facilitated the emergence of the new section of medicine: *radiology*.

In Russia, the first roentgenograms (X-ray films) were obtained in the physics laboratories of St. Petersburg (12–13 January 1896) and Moscow (15–16 January 1896). The first Russian X-ray machine for medical diagnostics was designed by A.S. Popov at the end of February 1896, set up in the Krondshtadt Sea Hospital.

At the beginning of the twentieth century, X-ray machines were available in many Russian cities: St. Petersburg (St. Petersburg University, the St. Petersburg Military Medical Academy, and the Clinical Institute of St. Petersburg), Moscow (the Moscow University), Kiev (St. Vladimir's Imperial University) and Kazan, among others. In 1896, in St. Petersburg's Military Medical Academy and in the Surgical Clinic of the Kiev University, the first operations were performed in the removal of foreign bodies, detected with the help of radiography.

The first issue of the radiological magazine, *Herald of Radiology*, was produced in July 1907 in Odessa, and the first all-Russian Congress of Radiologists took place in Moscow in December 1916; thus, radiology became an independent speciality in Russia. The State Radiological and Cancer Institute was founded in 1918 in St. Petersburg; its first president was the well-known physicist A.F. Ioffe.

After a year, the Physics Department of the Institute became an independent institution, the Institute of Radiology and Roentgenology, and M.I. Nemenov was appointed to the position of its director. In front of the Institute, on 29 January 1920, the first-ever monument dedicated to Roentgen was erected. The first radiological clinic was established in the Institute; later, similar clinics emerged in Paris's Curie Institute and in the Forsell Institute in Stockholm.

In 1919, the Russian Association of Radiologists and Roentgenologists was founded, and in 1920, the journal *Herald of Roentgenology and Radiology* was issued, which continues to be published today.

1.2 History of Russian Neuroradiology

The history of Russian neuroradiology began with a perspicacious prediction by V.M. Bekhterev, the outstanding Russian neuropathologist. In his presentation on 15 February 1896 in The Clinic of Central Nervous System Diseases, St. Petersburg Military Medical Academy, he told the audience that many diseases of the nerves are caused by changes in the skull and vertebrae and, possibly, X-rays could help to detect these changes. He foresaw visualisation of the paths of intracranial arteries through the skull, with the help of administration of a special substance that absorbs X-rays. He also envisaged the visualisation of a grey matter with X-rays. His predictions have come to fruition today in widely used neuroradiology methods like angiography and computer tomography (CT).

V.M. Bekhterev organised the first Russian neuroradiology department in the St. Petersburg Institute, which now bears his name.

Russian neuroradiology passed through the same stages as the world's neuroradiology. Its development was prompted by the general rise of radiological science and practice, and was further stimulated by the organisation of special neurological, neurosurgical and neuropsychiatric institutions, in which the first specialised neuroradiology departments were formed. Such prominent scientists as N.N. Altgauzen, M.D. Galperin, M.B. Kopylov and F.A. Serbinenko (1974), among others, played leading roles in the formation and prospering of Russian neuroradiology.

The 1920s was an epoch of pneumoencephalography development.

The 1930s were marked by the emergence of brain vessel angiography. The first angiography in Russia was performed in 1930 in the Narkomzdrav Neurosurgery Clinic in Moscow by B.G. Egorov and M.B. Kopylov. They used 25% iodide sodium solution in the procedure. In 1931, with the help of angiography, a traumatic aneurysm of the carotid artery was diagnosed in the same clinic. (Later, the Clinic was reorganised as the Neurosurgery Scientific-Research Institute, which is now the Burdenko Neurosurgical Institute). It was the first clinical case of vessel lesion diagnosis in Russia.

In 1965, A.I. Arutiunov and V.N. Kornienko, for the first time in Russia, started to use total angiography of brain vessels with femoral artery catheterisation (Aroutiunov 1971). In 1971, F.A. Serbinenko pioneered the method of radioendovasal occlusion of brain arteries, with the help of detached balloon. This method was subsequently named after him: the Serbinenko method.

The history of neuroradiology is, on the one hand, the history of collaboration of radiologists, neurologists and neurosurgeons in the development of clinical methods of central nervous system (CNS) radiological examination. On the other hand, it is the history of collaboration of physicists, mathematicians, engineers and radiologists in the design and creation of new devices for brain and diagnostics of spinal cord diseases.

The 1930s witnessed the arrival of linear tomography methods (*tomos* is the Greek word meaning "section") in radiology. Independently from B. Ziedses des Plantes, the Russian scientist V.I. Feoktistov considered the theoretical opportunity of capture of an object's internal layer on X-ray film in the course of synchronous moving of a tube and a film relative to the motionless isocenter during the objects exposure to the radiation (Feoktistov 1935).

From 1935 to 1946, the phenomenon of a nuclear magnetic resonance was discovered. In 1941, E.K. Zavojsky, in Kazakhstan, obtained one of the first nuclear magnetic resonance spectrum of a substance (Zavojsky 1945). The 1950s and 1960s witnessed a quest for practical solutions of tomography problems in neuroradiology, and the subsequent development of electronics and computer techniques. The 1970s and 1980s for Russian neuroradiology were the time of wide introduction of a CT method in the clinical setting, and the appearance of the first magnetic resonance scanners.

In the Soviet Union, the first computed tomograph manufactured by EMI (London) was set up in the Scientific Research Institute of Neurology in which, on 21 June 1977, the first CT brain examination in Russia was performed. The first second-generation scanner ND8000 (CGR, La Rochelle, France) was set up in 1978 in the Burdenko Moscow Neurosurgical Institute. In 1985, A.N. Konovalov and V.N. Kornienko published the monograph *Computed Tomography in the Neurosurgery Clinic*, in which they summarised the experience of CT use at the Institute of Neurosurgery. For the period from 1981 to 1985, more than 12,000 patients were examined in the Institute; in the overwhelming majority of them, the initial diagnosis set with the help of CT was later confirmed during the operations. The first Soviet CT scanners of the second generation were made in Kiev.

The first MRI scanner produced by Bruker, with the induction of the magnetic field of 0.22 T, was established in the Institute of Cable Industry, Moscow, in 1983. By the end of twentieth century, magnetic resonance imaging (MRI) had been strongly incorporated into a clinical practice, and in some cases (spinal cord examination) became a method of a choice in comparison with the usual CT. The high tissue resolution and a wide variety of types of contrast for MR images are typical for MRI.

Currently, MRI employs several physical factors defining the brightness of tissue on the image such as: proton density; T_1, T_2, and T_2^* relaxation time of protons in tissue; the movement of protons in the large vessels with a blood–cerebrospinal fluid (CSF) flow and passage of protons through a capillary net; random thermal water molecule motion; anisotropy of the diffusion proton motion and a magnetic susceptibility of tissues; and chemical shift of proton's resonance frequency in molecular complexes.

More importantly, volumetric CT and super-fast MRI open wide diagnostic opportunities of CNS examination not only

on a level of anatomic structures (simulation and support of surgery, endoscopy), but also on a level of molecular and gene biology. Neuroradiology becomes a quantitative method of brain function examination, the method of monitoring, and prediction of the results of therapeutic treatment and surgical intervention of many diseases.

Currently, large, specialised neuroradiology departments exist in clinical research centres in Moscow and St. Petersburg. The general radiologists working in radiological departments of hospitals with neurosurgery and neurological or psychiatric departments deal with problems of CNS disease diagnostics. In Russia, the specialty, unfortunately, bears the name "ray diagnostics", and it includes all the different disciplines (specialities) dealing with various sorts of radiation (emanation): radiology (including CT and MRI), ultrasound diagnostic and radiotherapy (while there is internationally accepted division into radiology) and nuclear medicine, which more precisely reflects the subject (the essence of the matter). In 1990, a society of ray diagnostics was established in Russia.

The specialised training on neuroradiology is currently relatively simple: after graduation, a physician attends the special 6-month course on radiology, listens to lectures, and passes the exam on main radiology topics including neuroradiology. Large neurosurgery centres have a specialised 2-year residence on radiology, in which physicians can combine the practical neuroradiological work (from X-ray images description to work on CT and MRI and conducting such diagnostic examination like direct angiography and myelography) with scientific research.

Recently, the educational process (from university to the obtainment of neuroradiology qualification) underwent revision in the light of international experience. Russian still lacks a neuroradiological society. In 2001, the Russia Academy of Medical Sciences established neuroradiology as a separate speciality.

The Moscow Institute of Neurosurgery (now The Burdenko Neurosurgical Institute) was founded in 1932, based on the Neurosurgery Clinic of the State X-ray (Roentgen) Institute of Russian Ministry of Health. The academician N.N. Burdenko was the Institute organiser and he became its first director. True to his plan, the Institute was created as a complex establishment in which neurologists, radiologists, morphologists, physiologists, ophthalmologists, otolaryngologists, psychologists, and other physicians worked together with neurosurgeons. The Institute's departments and laboratories promoted the development of such new scientific disciplines as neuroradiology, oto-ophthalmoneurology and paediatric neurosurgery, and helped to develop not only the practice, but also the theory of neurosurgery.

In different years, prominent Russian neurosurgeons B.G. Egorov, A.I. Aroutiunov, A.A. Arendt, L.A. Korejsha, V.M. Ugrjumov, S.S. Brjusova, and neuroradiologists M.B. Kopylov, A.N. Kun, Z.N Poljanker and A.S. Plevako, among other scientists and experts, worked in the Institute.

Currently, the Institute is the largest neurosurgery centre in Russia and, in fact, the world. There are three Members and Corresponding Members of the Russian Academy of Medical Sciences, more than 40 professors, and more than 100 Ph.D.'s among the more than 2,000 Institute staff. Since 1975, the Institute has been headed by the Member of Russian Academy of Science and Russian Academy of Medical Science Professor, A.N. Konovalov. The Institute is situated in a newly built, specialised surgical complex. In this 14-story building, there are ten various clinical departments and 300 beds. The surgical unit consists of 16 operating rooms. About 5,000 complex surgeries concerning central and peripheral nervous system disorders/diseases are annually performed in the Institute. The Department of Neuroradiology is equipped by six CT scanners (three of them being spiral scanners) and three MRI scanners (with magnetic field inductions of 1,0 and 1.5 T). The department has two analogue–digital angiography (DSA) devices. Standard X-ray machines use digital carriers to record X-ray images. All diagnostic devices and installations are linked by a special informational neuroradiological network that is connected with the general Institute's network and the Internet.

Further development of neuroradiology is closely linked with the increase of processing speed and improvements in computer technologies, increase of the (MRI) magnetic field induction, the development of "open" magnets for biopsy, the intra-operational control, the examination of critically ill patients and patients with complications after an injury, the children, and so forth.

1.3 New Functional Methods in Neuroradiology

The increase of the processing speed of CT and MRI scanners, the invention of new data-registration technologies and the algorithms of data-processing transfer neuroradiology to entire new level. Neuroradiology development the follows the path "from anatomy to brain functions" (Cha 2006). Anatomic scans of standard CT and MRI demonstrate different types of tissue: blood, fat, white and grey matter, bones, and so forth. Modern CT and MRI methods can estimate speed and orientation of diffusive motion of water molecules and "see" the tissues differ in exchange interaction of protons, transport of ions and molecules (K^+, Na^+), environmental pH and phagocytosis (Hesseltine et al. 2007; Spilt et al. 2006; Cha 2006).

With enriched blood flow, MRI can detect areas of the brain having increased neuronal and metabolic activity, find areas of damage in the brain–blood barrier, make a quantitative assessment of microvascular permeability of brain tissue, evaluate the state of receptors on the cell surface as well as hormonal activity, and reveal the presence of certain antigen and protein structures, among other abilities (Chai et al. 2007; Stadlbauer et al. 2007; Hourani et al. 2006; Holshouser et al. 2006; Cha et al. 2006). Thus, CT and MRI perform diagnostics not only on a cellular, but also on a molecular level. As such, diffusion, perfusion, and functional MRI and MR spectroscopy belong to the so-called methods of molecular visualisation.

1.3.1 Methods of Diffusion Motion Visualisation

Diffusion is the basic physical process occurring during the cell's metabolic reactions. Kinetic energy leads to Brownian motion (random walk) of molecules (thermal motion; the speed is about 10^{-3} mm²/s). As a whole, the molecular motion of protons in physiological systems is divided into three types: (1) movement with moderate speed in macroscopic vessels (about 10–100 mm/s); (2) slow flow in a capillary net, or perfusion (the speed is about 0.1–10 mm/s); and (3) diffusion motion of molecules (the speed is about 10^{-3} mm²/s). Blood flow in large vessels is measured as a volume-in-time unit, perfusion flow (a local blood flow) is measured as the volume of blood passing in and out of a given tissue weight (volume) per unit of time and the diffusion factor is estimated by the average square of the distance made by molecules for a time unit.

Phenomenologically, the diffusion properties in the isotropic environment is characterised with the help of Fick's law, which connects the vector of particle flux with the gradient of their concentration. The diffusion factor (coefficient), D, is a factor of proportionality. The higher the value of diffusion factor, the more quickly solution mixing occurs.

A. Einstein in 1905 applied the probabilistic approach to the description of diffusive motion. According to such approach, the cumulative motion of all particles is characterised by the probability of displacement of separate molecules from one point of space to another, although the exact trajectory (trace) of each particle is unknown. For a one-dimensional case and the isotropic environment, the displacement dispersion, x^2, is connected with the diffusion factor D and diffusion time, t, by Einstein's formula: $x^2 = 2\,Dt$.

The higher the value of diffusion factor, the longer an average distance of particle's displacement (within the same time). The diffusion coefficient unit of measurement is meters squared per second—the square of the circle where the particle would be in 1 s. In the simple experiment (Fig. 1.1), the drop of paint in water always colour produced a coloured circle, and the radius of this circle infinitely grows with a time (Fig. 1.1a). In the case of impenetrable, closed border, the painted area will not grow outside this border (Fig. 1.1b).

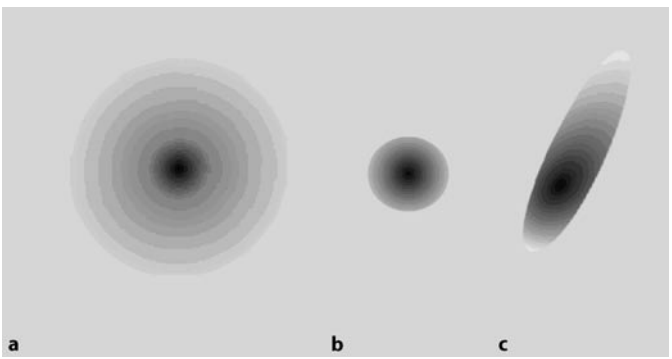

Fig. 1.1a–c Schema of the experiment with drops of paint: types of diffusion motion. **a** Free diffusion, **b** uniformly limited diffusion (isotropy), **c** non-uniformly limited diffusion (anisotropy)

In the case of presence of obstacles on the water surface, the paint particles bypass them, and the painted area has an elliptic form (Fig. 1.1c). Thus, after awhile since the beginning of the experiment, the painted area is characterised by the size of the spot, its form, and its orientation on the plane.

In a three-dimensional case, the law of displacement probability density is set by probability of particle transition in time t from one point, r_0, to another point, r. In the simple case of free diffusion in an unlimited, isotropic, and homogeneous environment, this probability has a Gaussian distribution. The volume in which a particle would be contained in time t is sphere with the centre in r_0; in the case of the limited isotropic diffusion, the sphere radius would not increase since some moment of time, and in cases of anisotropy or particle speed dependence from the motion direction, the sphere becomes ellipsoid.

1.3.1.1 Diffusion-Weighted MRI

The motion of the water molecule in live tissues occurs within the cell limits (the limited diffusion), as well as in intercellular spaces among structures, which restrict the molecules motion but still leaves them some freedom for manoeuvring between obstacles (the complicated diffusion). The term of measured or apparent diffusion coefficient was introduced to characterise the diffusion proton motion in a complex environment.

Generally, this value depends on the structure and microstructure of substance, in which the water molecules are diffusing: $D = 2.5 \times 10^{-3}$ mm²/s in free water at body temperature (Tanner 1970). In the real biological environment, water molecules can encounter natural barriers, such as like cellular membranes and large albumin molecules, which that interfere with free motion of protons. Therefore, in practice, the apparent diffusion coefficient is calculated, and its value is lower than diffusion coefficient for pure water at temperature.

The first diffusion-weighted MRI (DWI) was done in 1985 (Le Bihan et al. 1985). DWI was introduced into clinical practice together with third-generation MRI scanners (Le Bihan 1991). Spin echo-echo planar pulse sequences (SE-EPI) with two diffusion gradients (DG) of the same amplitude (G) and duration $-\delta$ are used to obtain DWI images. It is possible to apply DG in different directions, for example, in a direction of one of coordinate axes. The degree of weighting signal on diffusion rate is set by the value of the so-called diffusion factor, b, which is a parameter of the pulse sequence timing and depends on DG duration and delay time between them: $b = \gamma^2 G^2 \delta^2 (\Delta - \delta/3)$.

In this formula, γ is the gyromagnetic ratio, G the amplitude, δ is the duration of each diffusion gradient and Δ is a delay between diffusion gradients. The diffusion factor b is measured in seconds per squared millimetre. The measurements in DWI are performed two times, first with $b = 0$ s/mm² and then with $b = (500–7{,}000)$ s/mm². DG applied along the direction of each coordinate axes of the scanner are x, y and z in DWI. In diffusion tensor MRI (DTI) measurements are performed (at least) in six DG directions.

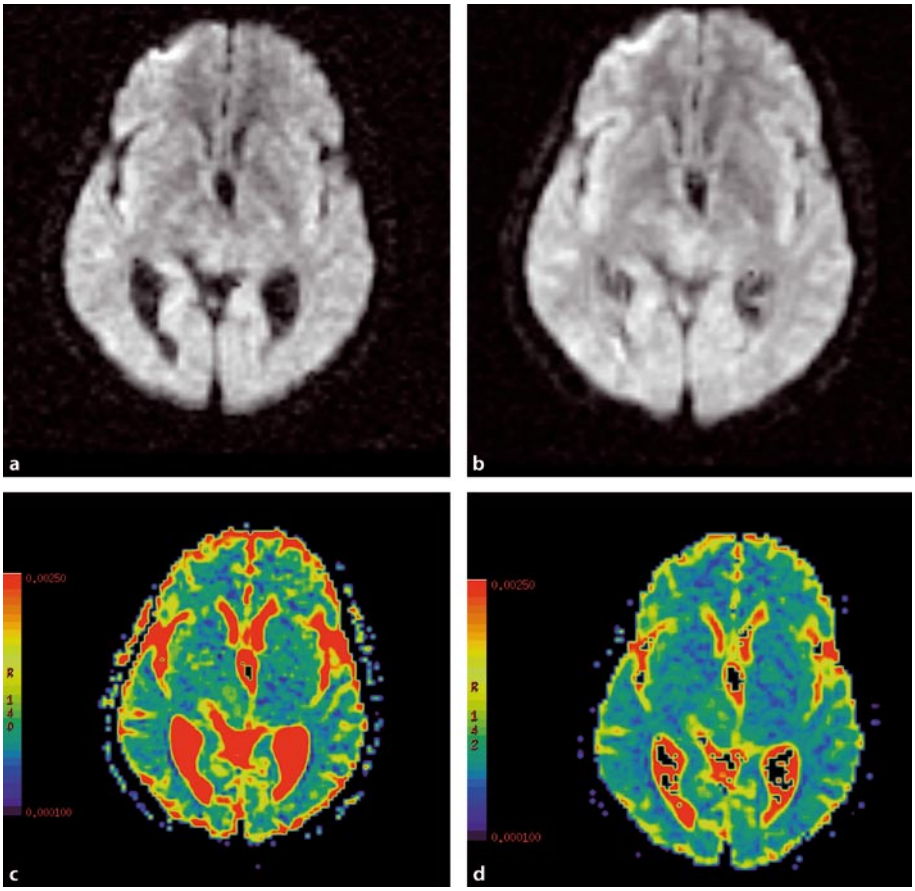

Fig. 1.2a–d DWI (combined series), obtained with $b = 500$ s/mm² (**a**) and $b = 1{,}000$ s/mm² (**b**). **c**,**d** ADC maps for the same scans

The phase changes caused by the DG, in stationary protons (very low diffusivity) in the structure of macromolecules, are completely compensated by the moment of registration. MR signal from such protons corresponds to T_2 of the tissue and is equal to a signal registered in SE-EPI sequence at $b = 0$ s/mm². The protons participating in diffusion motion with water molecules get the additional phase, and MR signal from them is lowered. Diffusivity of water in a tissue is visually estimated by the degree of MR signal attenuation on DWI.

In our examination, the gradient fields with amplitudes of $G = 11$ and 22 mT/m were used, which corresponds to diffusion factor values of $b = 500$ and 1,000 s/mm², respectively. For each DWI–EPI examination, we obtain five series of scan images: one series is a T_2 MRI; three at a supply diffusion gradient on each direction (x: anterior–posterior, y: right–left, and z: superior–inferior); and one, the so-called combined series for average diffusion coefficient (ADC) calculation, without taking into account the anisotropy in a tissue.

In Fig. 1.2a,b, the DWI (the combined series) is shown. These images were obtained at $b = 500$ s/mm² (Fig. 1.2a) and 1,000 s/mm² (Fig. 1.2b). The visible (by eye) decrease in MR signal intensity occurs in the case of the phase signal changing in one or two times. It is possible to estimate fast proton diffusion with the ADC of 5×10^{-3} s/mm² for $b = 500$ s/mm². For $b = 1{,}000$ s/mm², the optimum conditions for MR signal decrease visualisation would be for the protons diffusing more slowly, with the ADC on or about the order of 2.5×10^{-3} s/mm², i.e. almost the same as in free water. With even higher b values, it is possible to estimate the speed of diffusion motion in cell compartments (Le Bihan 2002). For a quantitative estimation of diffusion water properties in tissue, the parametrical diffusion maps are built on the colour of each pixel as it corresponds to the ADC (Fig. 1.2c,d). On the diffusion map, tissues with high speeds of water diffusion have blue–black colours.

1.3.1.1.1 Diffusion Anisotropy

Diffusion anisotropy is a dependence on direction of molecular diffusion ability. The diffusion maps obtained at DG action (effect) on six different directions in the space at $b = 1{,}000$ s/mm² are shown in Fig. 1.3a–e, and diffusion coefficient maps in a direction of coordinate axes x, y and z are reflected in Fig. 1.3f,h. The anisotropy of diffusion characters of corpus callosum white matter is clearly visible on the images. Water molecules easily diffuse alongside nerve fibres; however, their motion in the transverse direction is limited by the impenetrable myelin membrane.

For the description of diffusion properties changing with a direction, mathematical tensors are used. The diffusion tensor is defined as:

$$\bar{D} = \begin{pmatrix} D_{xx} & D_{xy} & D_{xz} \\ D_{yx} & D_{yy} & D_{yz} \\ D_{zx} & D_{zy} & D_{zz} \end{pmatrix}$$

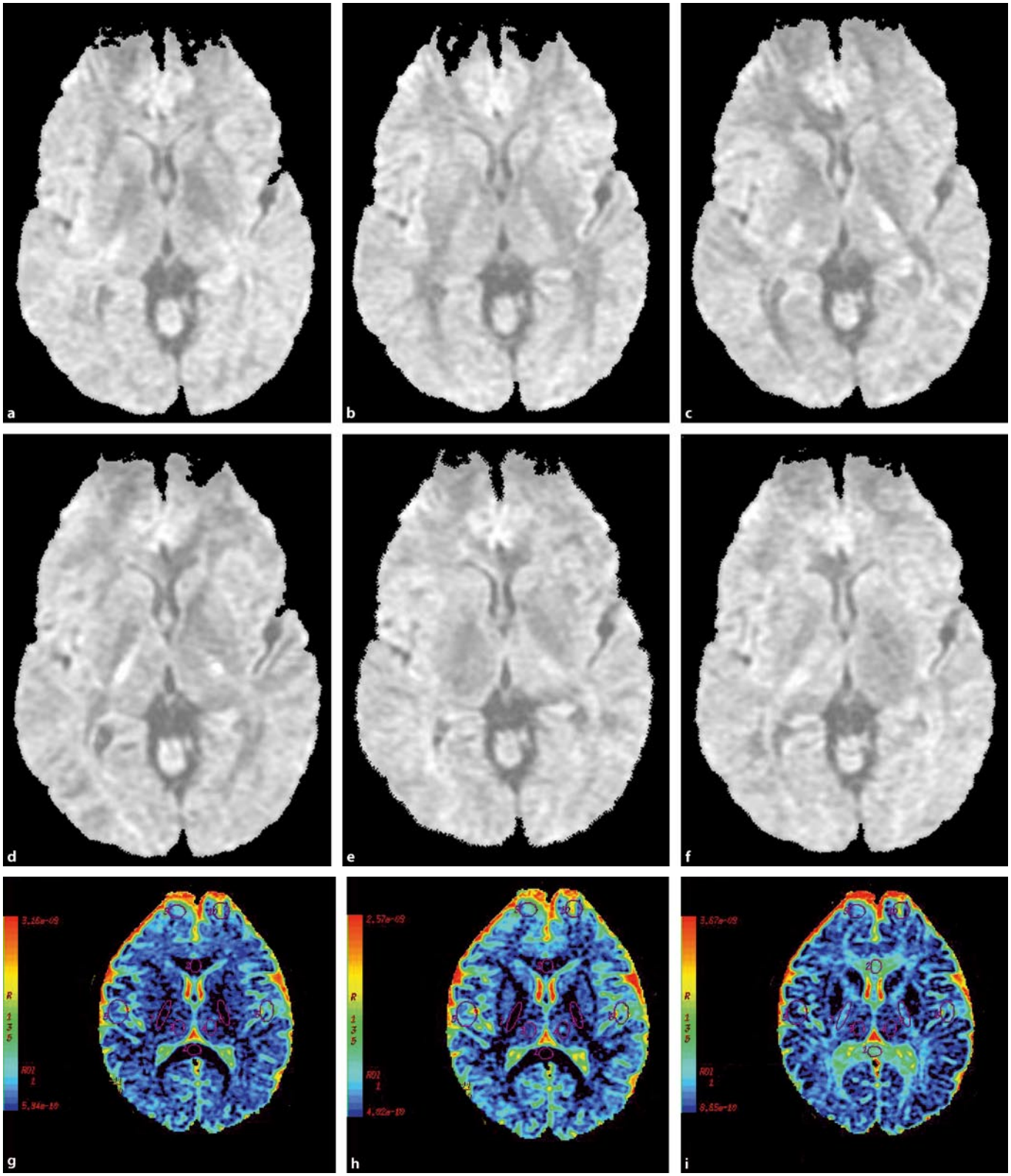

Fig. 1.3a–i DWI obtained at DG application at six different directions (**a**–**f**), and diffusion coefficient maps in a direction of coordinate axes *x* (**g**), *y* (**h**), and *z* (**i**)

The diffusion tensor is symmetrical, i.e. $D_{xy} = D_{yx}$, for any pair of indexes. This property reflects physical properties of the real environment, namely, diffusion properties would not change from the initial and final points of a diffusing molecule trajectory. Thanks to the diffusion tensor's symmetry, the six tensor coefficients (three diagonal and three non-diagonal) are sufficient for characterisation of diffusion properties of water molecules. Six coefficients of diffusion tensor define the form of a diffusion ellipsoid, its sizes and its orientation in space (Pierpaoli 1996; Mori and van Zijl 2002).

The diffusion isotropy means that diffusion motion of molecules does *not* depend on the orientation of environment, and during observation, the molecule would not leave the limits of sphere with a radius D, where $D = (D_{xx} + D_{yy} + D_{zz})/3 = ADC$.

Diffusion anisotropy assumes that, during the observation, due to orientation of environmental elements, the molecule would not leave the borders of the "diffusion ellipsoid" with half-axes λ_1 λ_2 and λ_3; here λ_1 λ_2 and λ_3 are the values of diffusion tensor (eigenvalues). The diffusion anisotropy can be quantitatively estimated with the use of the difference between the diffusion ellipsoid and the sphere with radius D_{cp}, for instance, with the help of the fractional anisotropy (FA) coefficient, relative anisotropy (RA) coefficient, index of anisotropy (IA) and so forth (Pierpaoli 1996). Diffusion tensor MRI (DTI) is used to visualise the anisotropy of water diffusion in the tissue.

In DTI, the line of nerve fibres forming the nerve tracts (paths) may be visualised via the diffusion ellipsoids' orientation, by connecting the vectors of diffusion tensor (Fig. 1.4). Connection algorithms are relatively complex, and therefore the various methods of calculation like structural modelling (structural modelling involves following the main diffusion directions), connective models (anatomical and functional connectivity), methods of integrated transformations and spherical harmonics (Q-space spherical harmonics), stochastic models (probabilistic models) and so forth are utilised (Mori and van Zijl 2002; Sen and Basser 2005; O'Donnell 2006).

These methods enable the tracing of multiple nerve fibres forming a neural tract; therefore, DTI is often called tractography—a demonstration of neural tracts visualisation. In the simple form, partial diffusion anisotropy is coded by colour, and visualisation of the direction of water molecule diffusion motion in tissue is carried out by colouring the pixels a certain colour, depending on orientation of their respective vector (red for the x axis, green for y and dark blue for z) (Fig. 1.5).

DTI is a tool of detection of structural communications between brain departments. Establishing such communication is especially important in the case of volumetric processes and the diseases deforming the anatomic structure or destroying white matter, such as tumours, brain injury, arteriovenous malformations, epilepsy and demyelinating diseases.) (Hesseltine et al. 2007; Holshouser 2006).

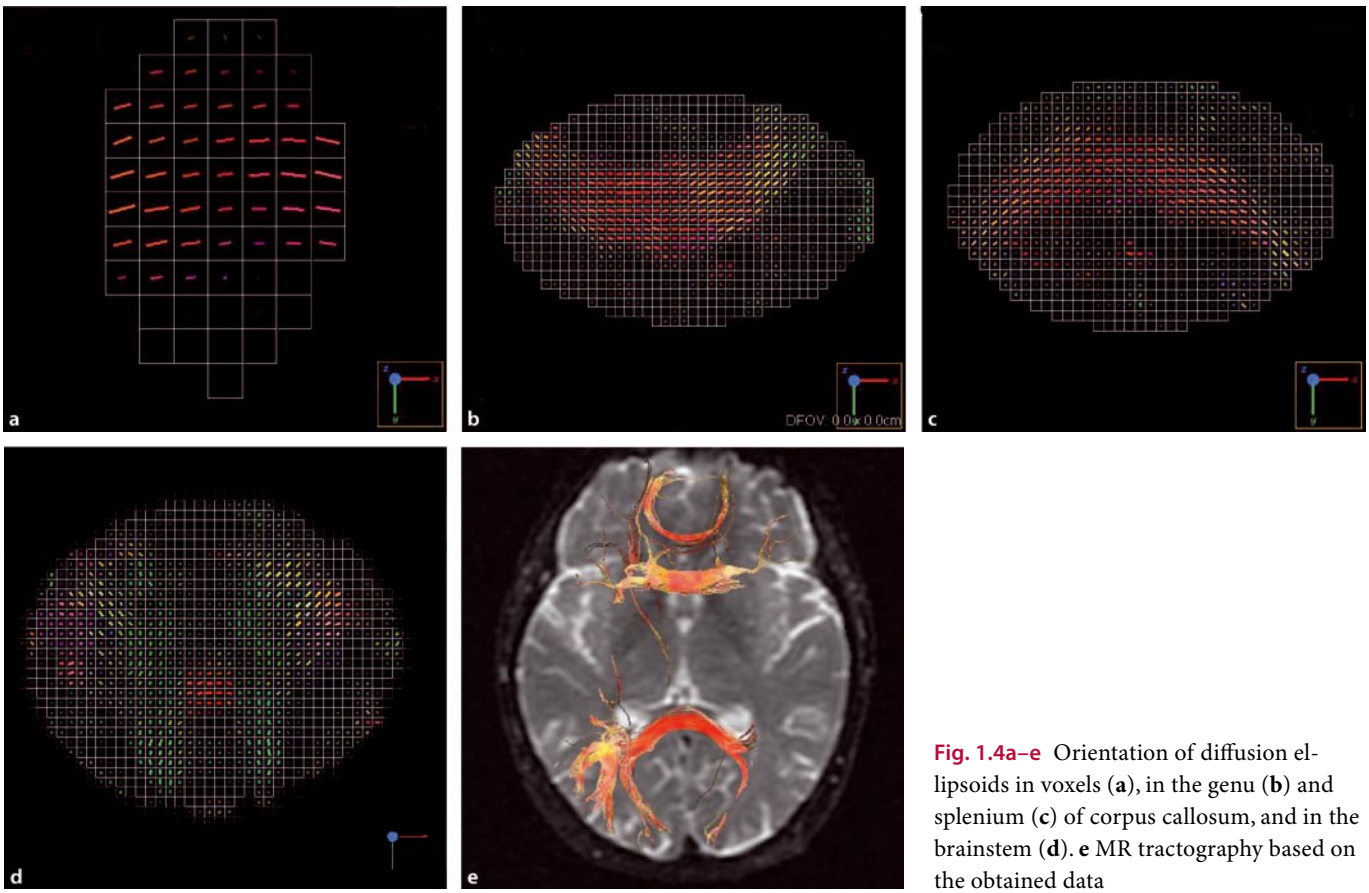

Fig. 1.4a–e Orientation of diffusion ellipsoids in voxels (**a**), in the genu (**b**) and splenium (**c**) of corpus callosum, and in the brainstem (**d**). **e** MR tractography based on the obtained data

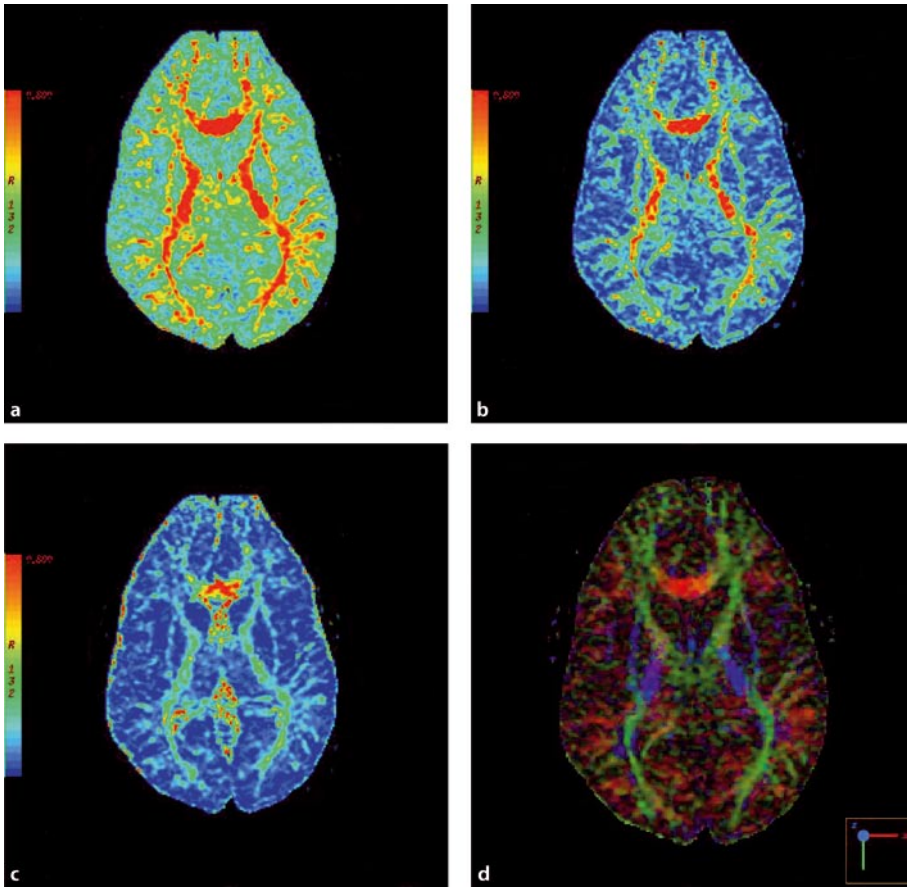

Fig. 1.5a–d Colour maps of anisotropy. The white matter conduction tracts (pathways) are marked by colour. **a** Map of partial anisotropy, **b** map of relative anisotropy, **c** map of anisotropy index, **d** structural map of anisotropy (according to the directions of the diffusion tensor vectors)

1.3.1.1.2 Clinical Application of DWI and DTI

Decrease in ADC speed in brain tissue is a sensitive indicator of presence and severity of ischaemic changes (Moseley et al. 1995). Today, DWI is one of the fastest and highly specific methods of early-phase ischaemic stroke diagnostics (within 6 h of onset), during which there is a therapeutic window for restoration of the affected brain tissue. In acute phase of stroke, the affected area on DWI typically has a high MR signal, whereas the surrounding tissues look dark. The ADC maps provide a reverse-in-brightness picture (Fig. 1.6). Diffusion ADC maps are a tool in ischaemia diagnostics and monitoring of stoke and subsequent chronic tissue degeneration caused by ischaemia.

Gradually, by the end of second week, the isointense signal from the affected area(s) replaces hyperintense one. Then the signal becomes hypointense, reflecting the focus of encephalomalacia. The high ADC values are observed in areas of chronic and old lacunar strokes. Currently, this method is perhaps unique, capable of detecting the new ischaemic area on the periphery of an old stroke zone (or widening the stroke area) in patients with newly developed focal neurological signs. Generally, the DWI non-invasiveness and swiftness predetermine its leading role in primary diagnostics of ischaemic stroke.

All diffusion-weighted examinations are performed without contrast administration. This is important for critically ill and restless patients, and especially for specialised examinations of brain development in children, beginning with the prenatal period. In the last case, DWI enables obtaining both the additional qualitative (visualisation) and quantitative tissue characteristics; it offers new opportunities of microstructure examination in the process of brain development (Konovalov 2001).

DWI and ADC maps provide additional diagnostic information for differentiation of neoplasms with similar signs on T_1 and T_2 MRI (glioma, tumours with ring-shaped contrast accumulation), peritumoral oedema (vasogenic or cytotoxic) and the presence or absence of intratumoral cysts, to name a few (Mulkern et al. 1999). At the same time, as our experience demonstrates, DWI data alone does not allow differentiation between benign astrocytoma and anaplastic tumours, or between anaplastic astrocytoma and glioblastoma (Kornienko et al. 2000). The information concerning the spreading of infiltrating and growing brain neoplasm is more interesting.

In many observations, the peripheral part of tumour (as a rule in the case of malignant glioma) is hyperintense on DWI; presumably it is linked with more dense cellular arrangement in the most actively growing tumour area (accordingly, there is a limitation on diffusive proton motion in this area). We used these data for planning the stereotactic biopsy with obligatory tissue sampling from this peripheral part of an intracerebral tumour.

DWI provides invaluable information for inflammatory lesion diagnostics of brain and spinal cord (abscesses, empyema) for the immediate time. Purulent abscess content has

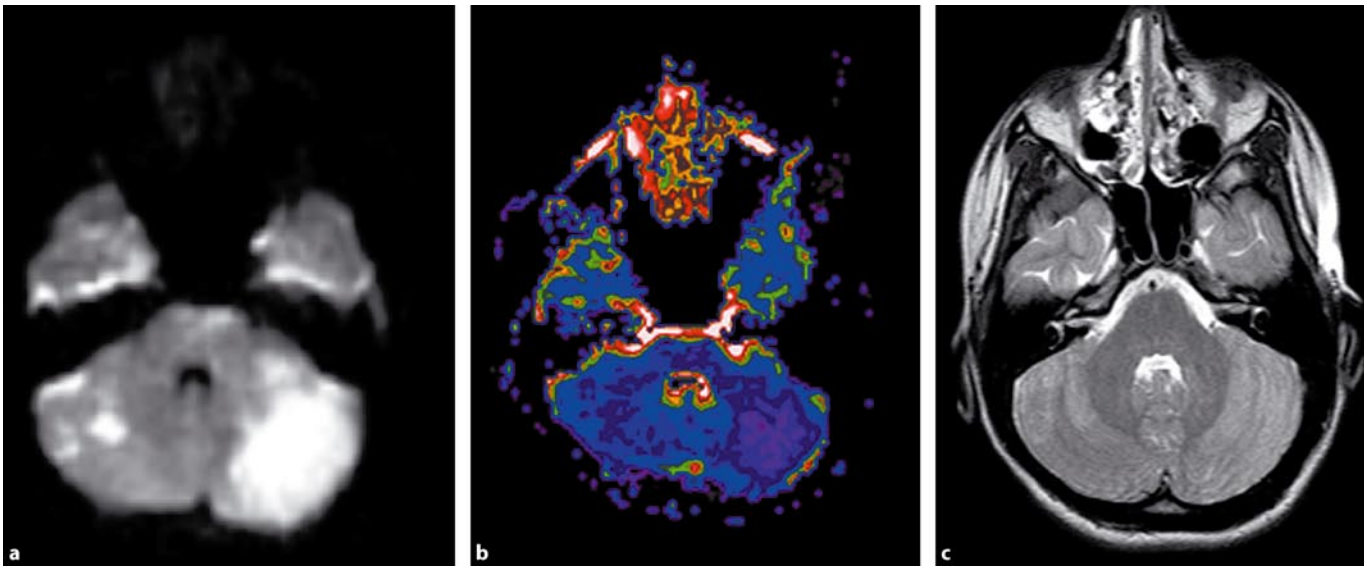

Fig. 1.6a–c Superacute phase of stroke. **a** The affected area has a hyperintense MR signal on DWI ($b = 1{,}000$), while normal brain tissues look dark. The regions of ischaemia in left and right hemispheres of cerebellum are violet (**b**). **c** T_2-weighted image: there are no MR signal alterations

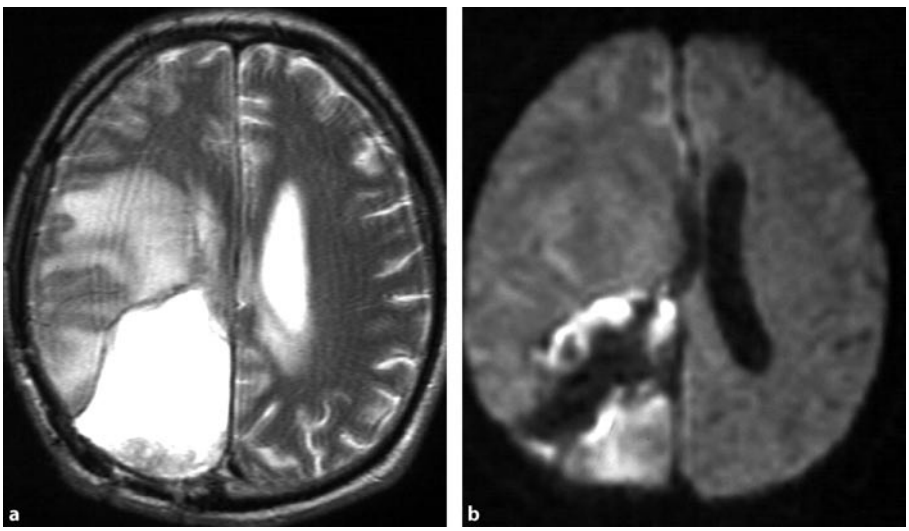

Fig. 1.7a,b Purulent complication after glioblastoma removal. **a** Wide operational defect MR T_2-weighted image. **b** DWI: the purulent layers (thickening) on the edges of defect are visualised (hyperintense MR signal)

a typical hyperintense MR signal on DWI and can be easily visualised on pretreatment (before draining) and as well on postoperative images. In addition, DWI can be used in the assessment of drainage intervention effectiveness or in the case of verification of the purulent complication in incision wound (Fig. 1.7).

The structural organisation properties of some new brain neoplasms—in particular, meningiomas and neurinomas—enable DWI to predict tumour histological type, with high reliability even before intervention. Based on this method data, the epidermoid and arachnoid cysts can be precisely differentiated.

Recently, DWI and DTI methods have begun to be applied to visualisation of a neural tract lines—tractography, especially in diagnosing white matter diseases caused by congenital metabolic defects, traumatic (diffusive axonal lesions), autoimmune, toxic and radiation damage (Lee et al. 2005) (Fig. 1.8).

Tractography is a new and promising technique that enables non-invasive viewing of the brain neural tracts (Batchelor et al. 2006). Despite some technical problems, the first results in tractography application to neurosurgery seem promising (Chepuri 2002). It is possible to plan operational access and to estimate the scope of brain hematoma to be removed, taking into account neural tracts and their involvement in the pathological process (dislocation–deformation, invasion, damage), with an aim to maximise the radical tumour resection and to minimise the subsequent complications (Stadlbauer et al. 2007).

The results confirm the value of a new diagnostic MR technique that enables increasing MRI specificity in establishing the correct histological diagnosis, and improves the accuracy

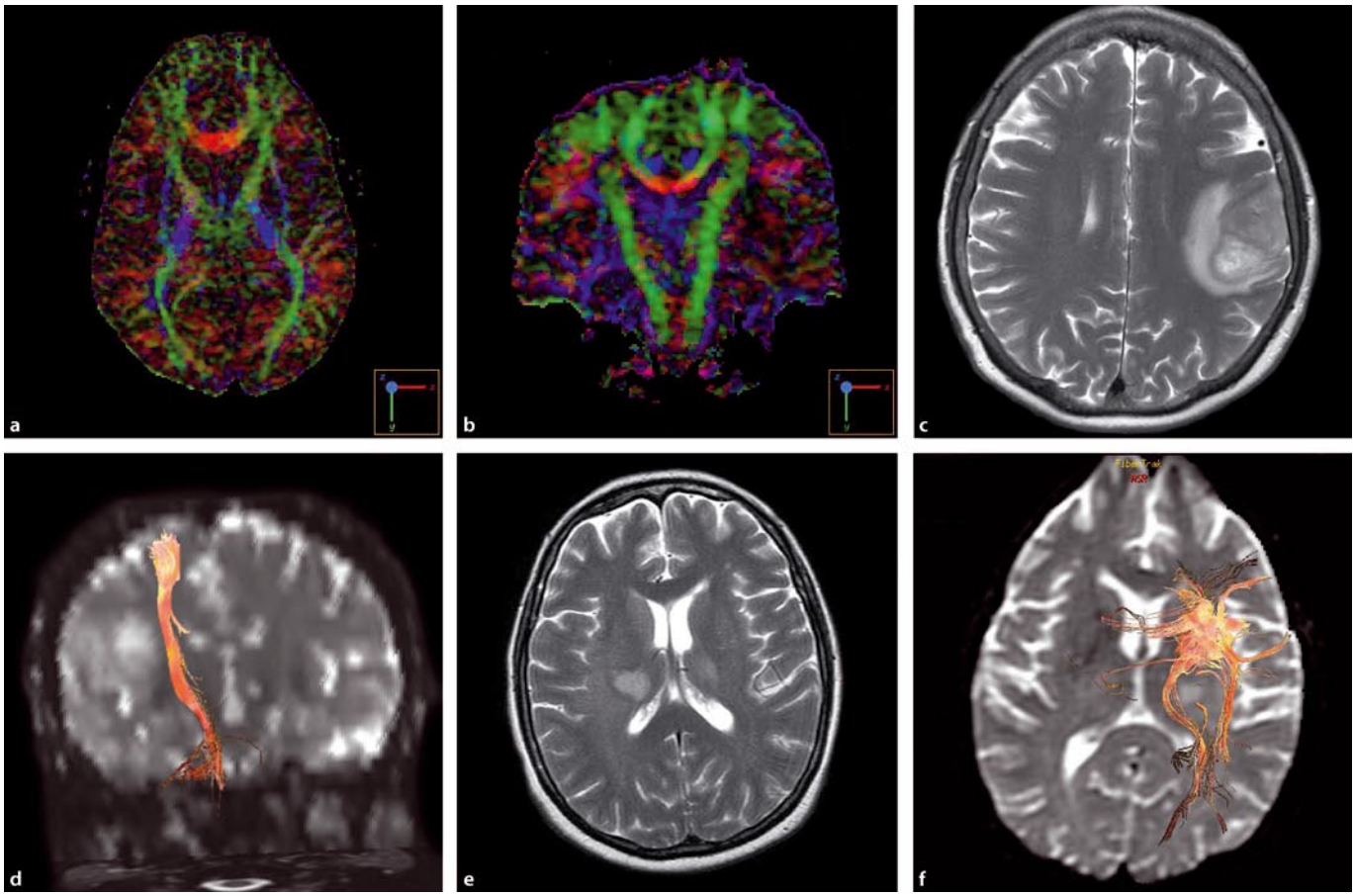

Fig. 1.8a–f MR tractography. **a** Axial projection, structural map. **b** Coronal projection, structural map. **c** T_2-weighted MRI, axial scan of patient with glioma. **d** Construction of the corticospinal tract in coronal plan in zone of tumour location. **e** T_2-weighted MRI of a patient with metastasis in basal ganglia. **f** Splitting of the nerve fibres around metastasis

of detecting the various components of tumour growth (tumour, infiltration and peritumoral oedema) and the borders of ischaemic lesion(s).

1.3.1.1.3 Perfusion Examinations

Methods of perfusion examination are used to consider and make quantitative estimation of the blood movement that supplies each element of organ or tissue volume. It is widely known that, unlike the majority of parenchymatous tissue, brain tissue does not accumulate glucose, and brain cells can produce energy via anaerobic glycolysis only for several minutes. Meanwhile, the brain consumes about 25% of all glucose consumed in the entire body, and for neurons, the uninterrupted and sufficient supply of oxygen and glucose is necessary. There are complex mechanisms of autoregulation that manage brain perfusion to satisfy the demands of the nervous system for energy (released in a course of metabolic processes).

There are several modern quantitative methods of brain haemodynamic examination: MRI, CT with contrast enhancement, CT with Xe, single-photon emission computed tomography (SPECT) imaging and positron emission tomography (PET). The obvious advantages of CT and MRI are minimally invasive, high sensitivity in tissue microcirculation assessment, high resolution, the short examination time (within the framework of standard protocols), and last, but not least, the reproducibility of results (Sorensen and Reimer 2000; Ting-Yim 2002; Cha 2006; Waaijer 2007).

The most widespread perfusion examination in neuroradiology is that performed based on intravenous bolus administration (CT and MRI). The dynamic studies of bolus passage demonstrate its distribution in tissue in each given image pixel, depending on time. The following main haemodynamic characteristics are used for quantitative assessment: cerebral blood flow (CBF), the cerebral blood volume (CBV) and mean transit time (MTT).

The blood flow characteristics are measured in the ratio to 100 g of brain tissue. Accordingly, the value of CBV is measured in millilitres per 100 g of brain tissue, and CBF is measured in millilitres per 100 g per minute. The local (regional) CBV is defined as percentage of blood volume in a single element of brain tissue volume. MTT is measured in seconds.

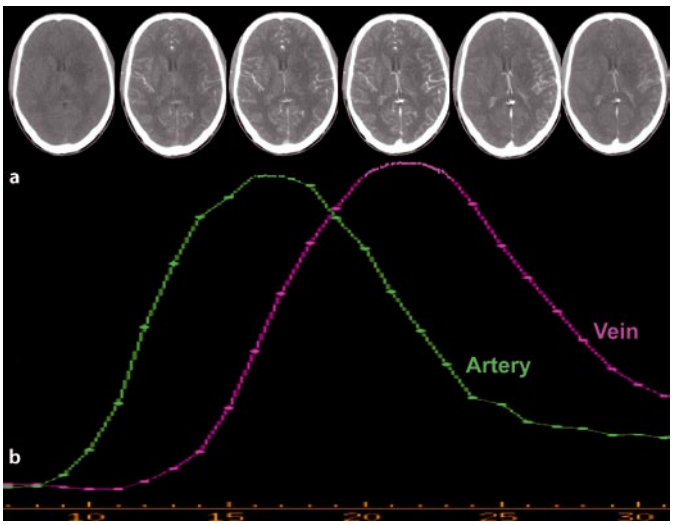

Fig. 1.9 Perfusion CT. **a** Series of dynamic CT scans, **b** the concentration–time curve in an artery and vein

1.3.1.1.4 Perfusion CT

The modern spiral CT scanners present new opportunities in tissue perfusion examination during the first passage of the iodide contrast bolus. This method has high resolution and provides quantitative assessments of tissue perfusion, and currently, it is one of the most perspective methods. Perfusion CT is based on analysing the CT density increase during contrast media passage through brain vascular structures. Contrast bolus (iodine agent with concentration 350–370 mg/ml, speed of administration is 4 ml/s) is administered intravenously. Spiral CT obtains a series of scans with 1-s intervals, within 50–60 s after contrast administration (Fig. 1.9).

1.4 Perfusion-Weighted Imaging

There are MRI methods of haemodynamic perfusion examination, aided by exogenous and endogenous markers:

- Contrast media (theory of non-diffusing markers, or central volume theory)
- Arterial spin labelling (kinetic theory of diffusing markers)
- Obtaining the images that depend on blood oxygenation level (BOLD)

The methods of perfusion assessment during contrast bolus passage are called perfusion-weighted MRI, or PWI. These examination methods are currently widely used in MR diagnostics, especially in combination with MR angiography and MR spectroscopy. PWI uses changes of T_1 or T_2 tissues contrast due to infusion of gadolinium into blood as a contrast agent. Normally, gadolinium does not pass through blood–brain barrier. It can pass into intracellular spaces only in cases of blood–brain barrier disruptions (Cha et al. 2007).

The usual MRCM (MR contrast media) concentration in bolus is 0.1 mmol/l—the same as in standard examinations with contrast enhancement. The CM bolus is administrated quickly (about 2–3 s); the speed of administration is 4–5 ml/s, and higher than in the standard infusion. After the bolus, a buffer solution is administrated. Ideally, the bolus envelope curve should have rectangular form. The bolus passage on consecutive (in time) scans corresponds with the sharp decrease of MR signal intensity. In the process of CM bolus passage through the vascular system, multiple registration of the image from the same location occurs (usually it is 10 different levels).

The scanning takes place for 1–2 min. The graph of intensity decrease during CM bolus passage provides the curve "signal intensity–time" in each pixel of the scan (Fig. 1.10). The form of this curve for arteries and veins provides arterial and venous function data; with the help of these data, the haemodynamic tissue parameters are calculated. The regional CBV (rCBV) is estimated on the basis of area under curve "concentration–time"; the MTT calculation is performed on the basis of centre of gravity in CM distribution position, regional CBF (rCBF) = rCBV/MTT. The perfusion maps are built in "off-line" mode in the specialised workstations.

PWI uses SE or gradient recalled echo (GRE) pulse sequences. The advantages of EPI-SE are the absence of geometrical distortions and good detection of arterial function in large arteries at the base of the skull. The main shortcoming is the echo time (T_E) of 40–80 ms, necessary for maintenance of T_2 weighting of the MR signal, which limits the time interval between scans. EPI-GRE provides time resolution of 1 s; however, it cannot obviate geometrical distortions.

The method of dynamic T_1 MRI is used in cases of examination of CM distribution in extracellular spaces. The time range of a dynamic curve in cases of T_1 examination is 3–5 min from the moment of CM administration. The CM passage through the vascular net is accompanied by increase of MR signal intensity in areas of CM accumulation. Dependence $S(t)$ is used for construction of the concentration–time curve, C_t. The steepness of the front of the CM accumulation curve (as well as in perfusion CT) characterises a local blood flow, maximum value of MR signal to local blood flow volume; the form of the concentration curve allows estimation of microvascular permeability of blood–brain barrier.

The advantage of perfusion examination with the help of the arterial spin labelling (ASL) method is the possibility of perfusion assessment without CM administration (Chai et al. 2007). The method is based on the proximal labelling of water protons with the help of presaturation. The "labelled" spins (they get the additional phase shift) enter (with the blood flow) the vascular brain bloodstream and account for the decrease of MR signal from microvascular structures on dynamic MRI series. The second series is registered in the absence of saturating radiofrequency pulse. The local blood flow is calculated on the difference between the two series (with presaturation and without).

Currently, two modifications of ASL are used, continuous (CASL) and pulsed (PASL). The duration of examination is 15 min in the field of about 1.5 T. The MR signal change due to spin labelling is lower than in the case of bolus CM admin-

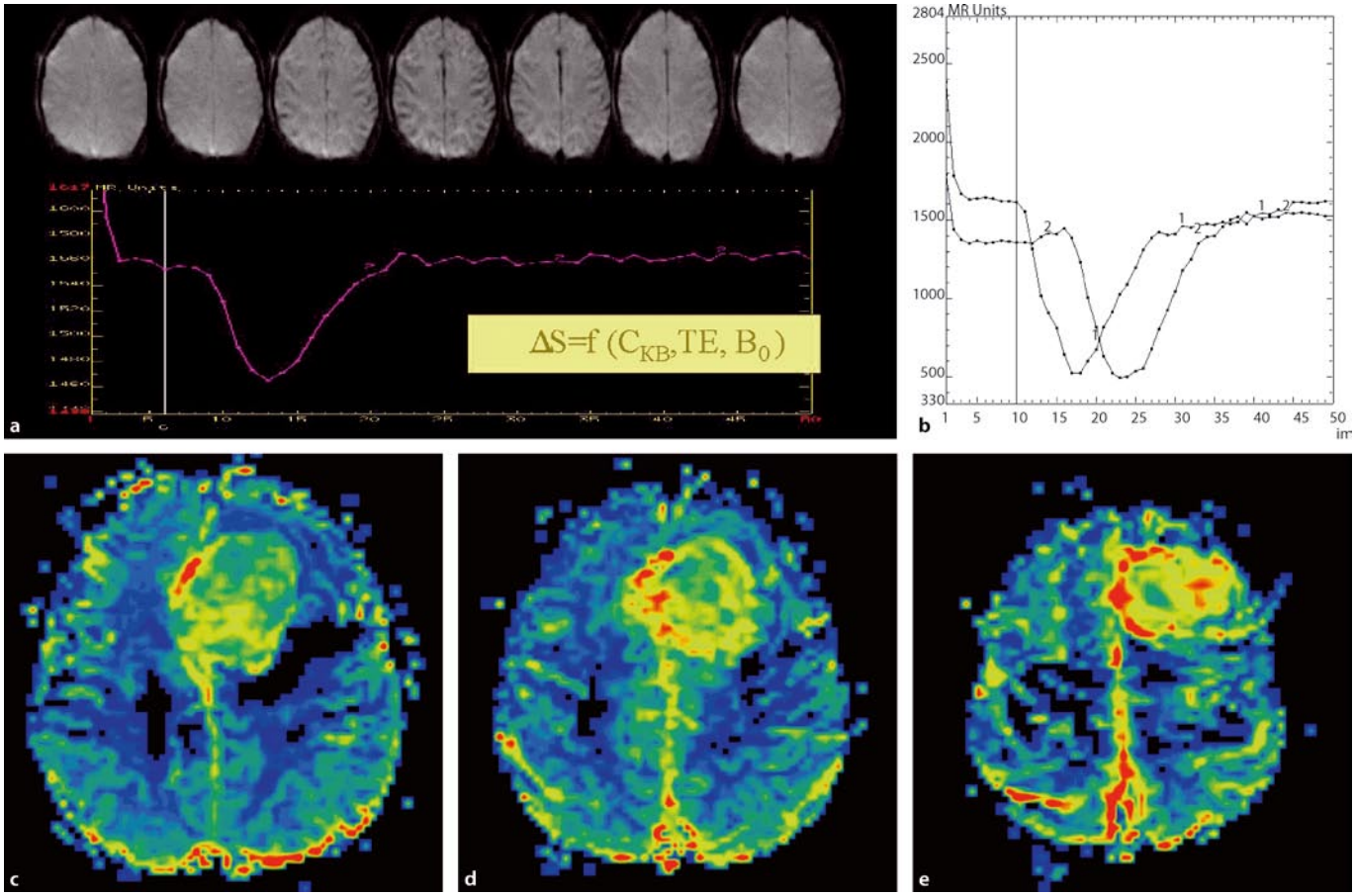

Fig. 1.10a–e Perfusion MRI. **a** Series of dynamic MRI and signal intensity–time curves in normal brain tissue. Patient with meningioma. **b** The signal intensity–time curve in an artery (*1*) and vein (*2*). **c–e** CBV maps on different levels

istration, and reaches only 15% of the latter (Alsop and Detre 1998). This method could gain recognition in the clinic, probably with the spreading of high-field MRI with the induction of 3 T or higher. Functional MRI (fMRI) utilises the magnetic properties of blood as an exogenous marker in magnetic field 1.5–3 T (discussed below).

1.4.1 Clinical Applications of CT and MRI Perfusion

Currently, perfusion examinations are performed to estimate the haemodynamic of brain tumours in cases of differential diagnostics of brain lesions; for tumour-state monitoring after chemo- and radiotherapy; in diagnostics of the tumour recurrence and radiation necrosis; and in cases of brain injury and CNS damage like ischaemia, hypoxia, large-arteries stenoses, blood diseases, vasculitis and moyamoya disease.

Epilepsy, migraine, vasospasm various mental diseases (including dementia), autism, and so forth, are prospective in terms of perfusion methods application.

CT and MRI perfusion allow building of parametric maps and quantitative characterisation of areas of hyper- and hypoperfusion, which is especially important in tumour and cerebrovascular disease diagnostics. Perfusion maps provide important additional information about characteristics of normal and pathological tissues (in areas of tumour, oedema, necrosis, and so forth).

In neurosurgery, PWI is used in primary differential diagnostics of malignancy levels of brain neoplasms, in particular gliomas. However, it is necessary to remember that perfusion CT and MRI do not allow specifically differentiating tumours according their histology, nor does it enable estimation of the tumour spreading into brain tissue. The hyperperfusion is focussed within the structure of astrocytoma; it can indicate increase of tumour malignancy because the perfusion level of tumour is related to the development of abnormal vascular net (angiogenesis) and thus, with the tumour's viability.

The abnormal vascular net in a tumour can be the evidence of its aggressiveness. In contrast, the decrease of perfusion in a tumour tissue under the influence of chemo- or radiotherapy can be a sign of response to treatment. Use of PWI in target selection for stereotactic intervention is helpful, especially in cases of gliomas that are characterised by full absence of contrast accumulation with the use of standard CT and MRI (Fig. 1.11).

PWI potential is higher in assessment of histological type and spreading of extracranial neoplasms than of intracranial ones (Fig. 1.12). PWI successfully visualises meningioma and

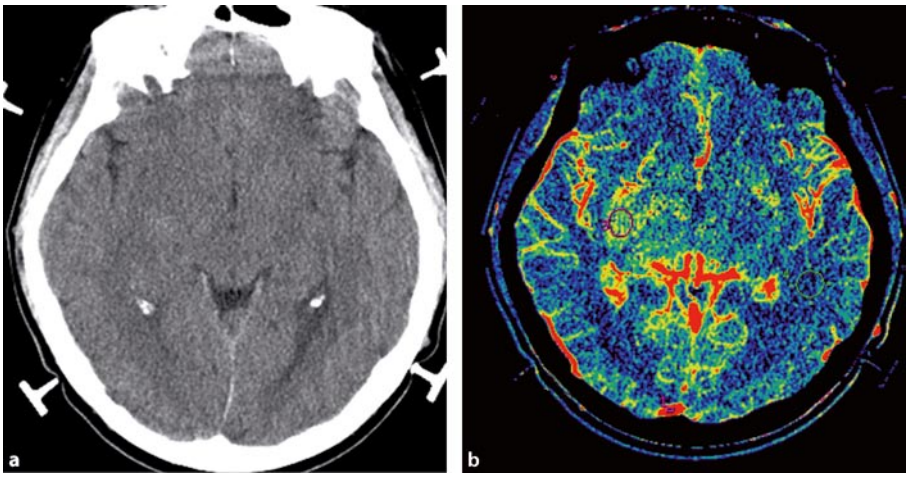

Fig. 1.11a,b Glioblastoma of right temporal lobe. **a** CT with contrast enhancement does not reveal its pathological accumulation. **b** CBV (based on CT data) map visualises the area of elevated perfusion: the site of biopsy is marked by a *circle* (region of interest [ROI] 3); CBV in the tumour increased more than three times in comparison with normal white matter (ROI 4)

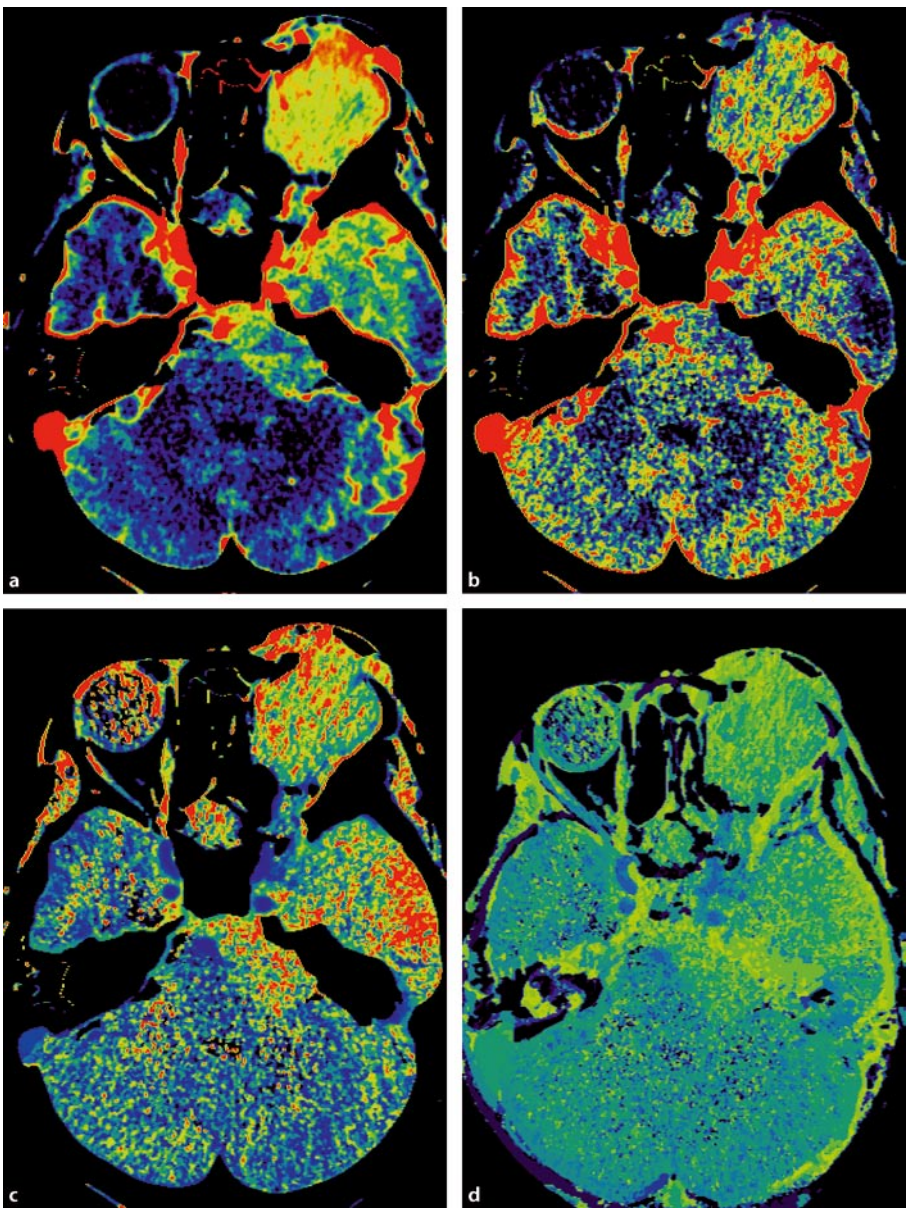

Fig. 1.12a–d Perfusion maps on the basis of skull. CT in patient with cranio-orbital meningioma. **a** CBV, **b** CBF, **c** MTT, **d** TP (time to pike)

neurinoma of cerebellopontine corners according to the high haemodynamic parameters in meningioangiomatoses. In addition, it was demonstrated that there is a clear correlation between local blood flow (CBF, CBV) and direct angiography data in patients with meningiomas (Fig. 1.13).

The tumours with radiopaque shadows in the early capillary phase of angiography have especially high perfusion, and such tumours are characterised by high risk of a intraoperational bleeding in the moment of extraction. CT PWI data are highly specific in demonstrating the blood supply of haemangiomas located in posterior cranial fossa; in this case, early and marked contrasting is combined with high perfusion.

PWI is used successfully in differential diagnostics of postoperative continued tumour growth and radionecrosis. In both cases, standard CT and MR examinations can show the accumulation of contrast in tissues, and in both cases, blood–brain barrier disruptions are observed. Blood–brain barrier disruptions cause CM extravasation in pathological tissues, with subsequent contrast accumulation. However, the pathophysiological reasons in both cases are different. For tumorous tissues, the perfusion increase or the reaching of normal perfusion level are typical, as in necrotic tissues the blood supply is absent.

Blood–brain barrier disruptions in cases of tumours are related to the invasive growth of tumour cells and vascular wall damage. In case of radionecrosis, the disruption of blood–brain barrier is an initial step, and it declares itself (unlike tumours) in the form of perfusion decrease (iso- or hypop-

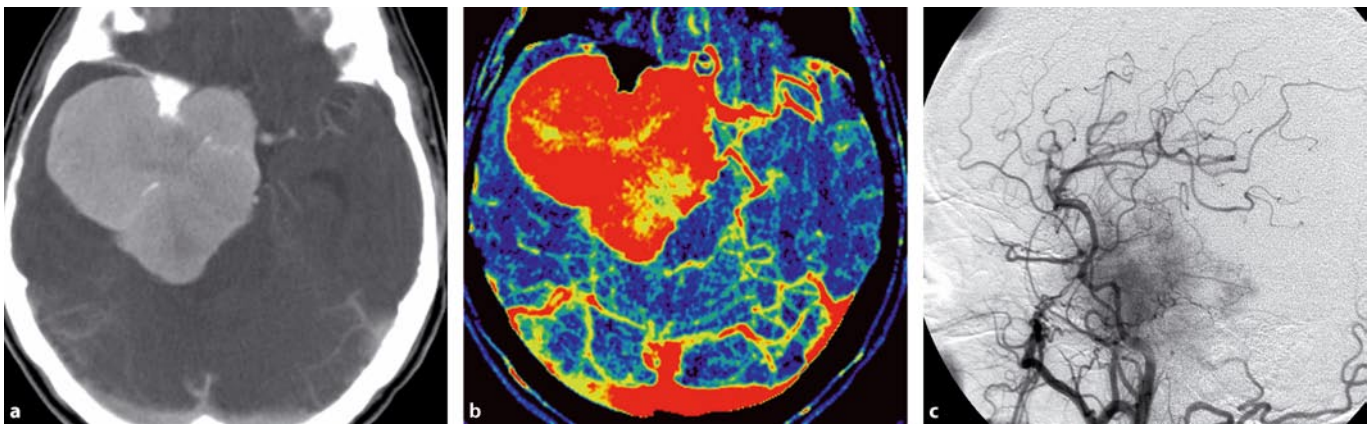

Fig. 1.13a–c Meningioma of sphenoid wing. **a** CT scan with contrast enhancement, **b** CBV map demonstrates the large tumour with high perfusion indicators, **c** direct angiography confirms the luxury meningioma blood supply in arterial phase

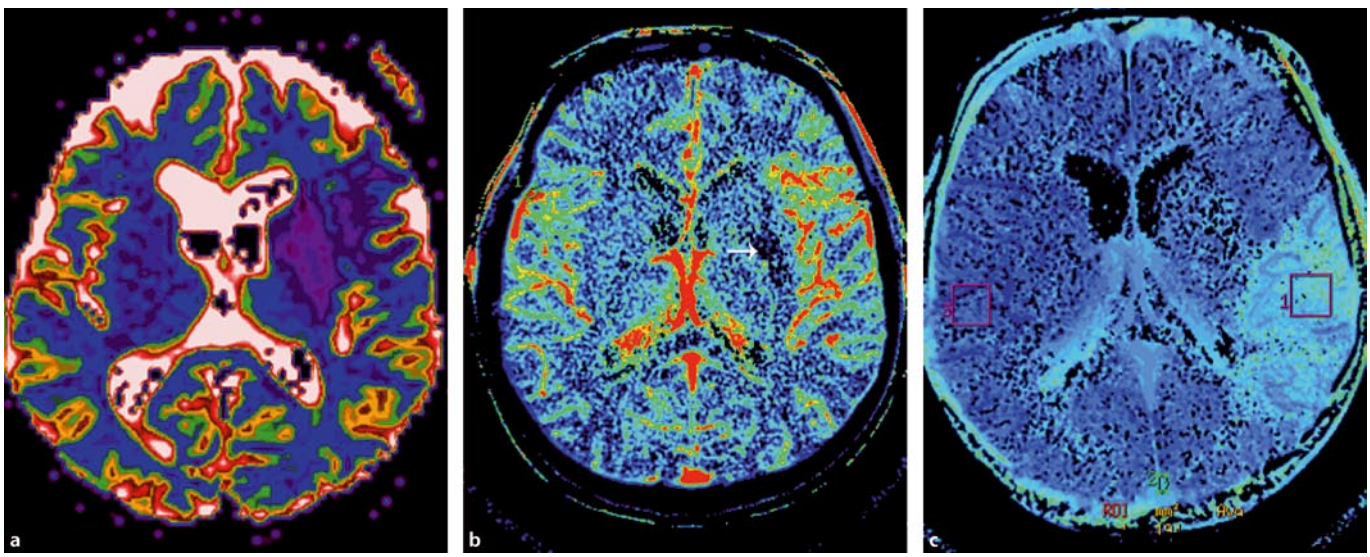

Fig. 1.14a–c Ischaemic stroke in left MCA territory. **a** ADC map (the stroke is coloured *violet-blue* and affects the basal ganglia), **b** CBF map: area of deep nucleus damage with very low cerebral blood flow parameters (*arrow*), **c** MTT map (the area of penumbra is marked by ROI 1, with *light blue*)

erfusion). The areas of radionecrosis appear as areas of weak blood filling on CBV maps. The time of CM bolus passage is longer than normal, as in cases of ischaemia.

Undoubtedly, ischaemic brain damage occupies first place in the frequency of PWI methods being used. Currently, PWI is an integral part of diagnostics in patients in whom cerebral ischaemia is suspected. The first clinical PWI application in brain lesion diagnostic in humans was performed for stroke diagnosis.

At present, perfusion MRI is, perhaps, the sole method of early ischaemia verification, capable of diagnosing the haemodynamic decrease in certain brain areas (as the main mechanism of ischaemic damage), even in the first minutes after appearance of focal neurological signs. The combination of PWI and DWI in patients with brain ischaemia enables detection of the heterogeneity of the ischaemic area(s), to distinguish the nuclear lesion (the area of necrosis) and so-called penumbra (the area of ischaemic half-shadow), with only functional changes (Fig. 1.14).

The new approach in PWI use is studying the haemodynamic shifts in brain substance in patients with severe stenosis and occlusion of large extracranial vessels. It turned out, for instance, that there is no clear correlation between stenosis level of internal carotid artery and perfusion decrease on the territory supplied by this artery. One of the main reasons for this is the development of collateral circulation with haemodynamic compensation. Generally, careful analysing of these data in vascular surgery leads to more accurate treatment selection for these patients; in particular it limits the indication for extracranial–intracranial shunting.

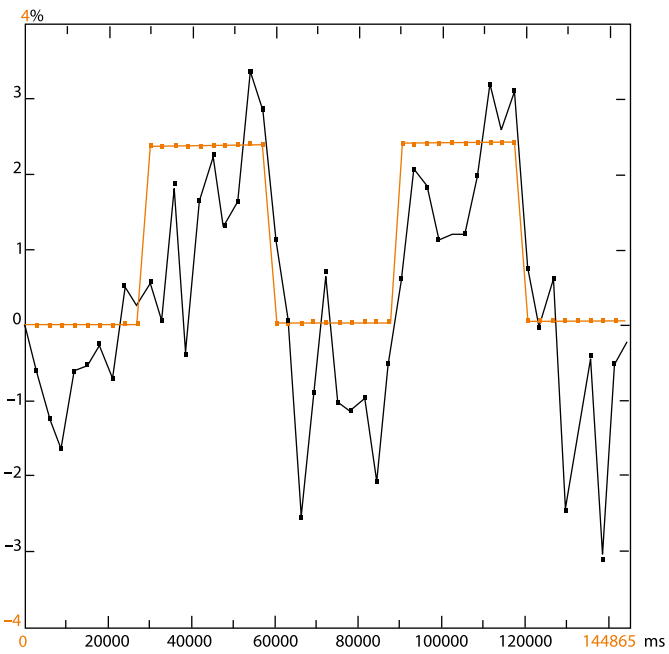

Fig. 1.15 Haemodynamic response of brain to the increase of neuronal activity for interchange of stimulus and rest periods

The use of perfusion CT and MR investigations in children for whom the vessels occlusions are rare (characterised by the small probability of vessels occlusion) is especially important. The hyperintense MR signal in T_2 consequence in most cases is caused not due to stroke, but to other reasons (for instance, vasogenic oedema, hypomyelinogenesis). PWI could indeed reveal the ischaemic area in children, for whom the small probability of stroke exists (Konovalov et al. 2001).

Another example of PWI use is arteriopathy studies in children. Reasons for this study include idiopathic (primary) and secondary vasculitis, the consequences of moyamoya disease, and sickle cell arteriopathy. For such diseases, perfusion MRI sensitivity is compatible with those of perfusion CT with Xe-133, and radionuclide methods. PWI has several advantages in anatomical damage visualisation and in detection of pathological and anomalous blood flow, observed, for instance, in cases of collateral circulation.

Revealing the pathological circulation in children is especially significant in situations of patient selection for surgical treatment of arteriopathy. The collateral circulation in children with arteriopathy can be extensive at the time of its primary detection. Dynamic perfusion MRI is used in cinema mode for perfusion-loop, revealing collateral circulation assessment, and time of CM passage to tissue estimation.

All this makes this method highly informative in detecting and subsequent observation of patients with moyamoya disease. It is considered that, at an initial stage of this disease, perfusion parametrical imaging demonstrates the increased blood flow in the basal ganglia area, altered peripheral cortical perfusion, deficit, or change of the CM passage time. These signs are typical for this disease.

1.5 Functional MRI

Brain activity mapping enables revealing of the areas of neuronal activation in response to tests, motor, sensor, and other stimulus. Until recently, similar mapping was performed with the help of radionuclide methods: PET and SPECT imaging.

Functional MRI (fMRI) is based on increase of brain haemodynamics in response to cortical neuronal activity due to certain stimulus (Ramsey 2002; Pouratian et al. 2003; Sunaert 2006).

BOLD EPI-GRE registers hyperintense MR signal from active areas of the brain cortex. The registration time of one MR image is about 100 ms. fMRI signal intensity, registered by physiological load, is compared with the intensity, registered in the event of its lack. During MRI examination, the stimulation periods (duration of 30 s) alternate with control periods (without stimulation) of the same duration (Fig. 1.15). The total number of scans registered during the examination reaches 20,000. This method of stimulus presenting is called a block paradigm.

The areas of statistically significant MR signal increasing during activation, revealed in the course of subsequent mathematical processing of images, correspond to areas of neuronal activity. They are marked with colour—this way the neuronal activity maps are built and these maps are im-

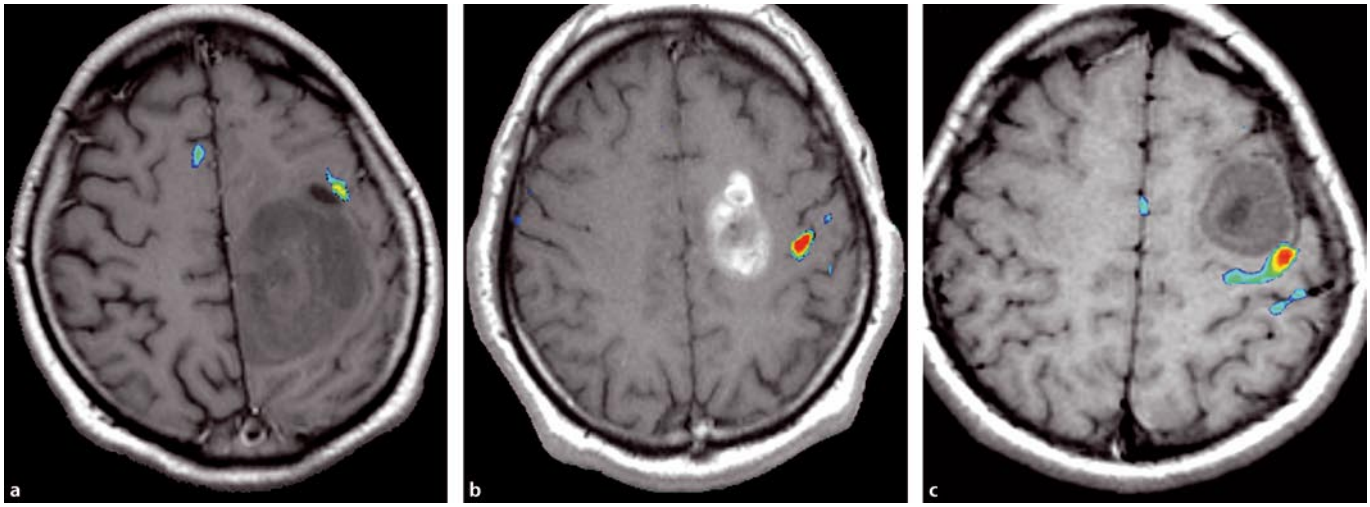

Fig. 1.16a–c fMRI neuronal activity maps of cortical motor centre activation in different patients with intrinsic tumours of the paracentral area, imposed on a T_1 image

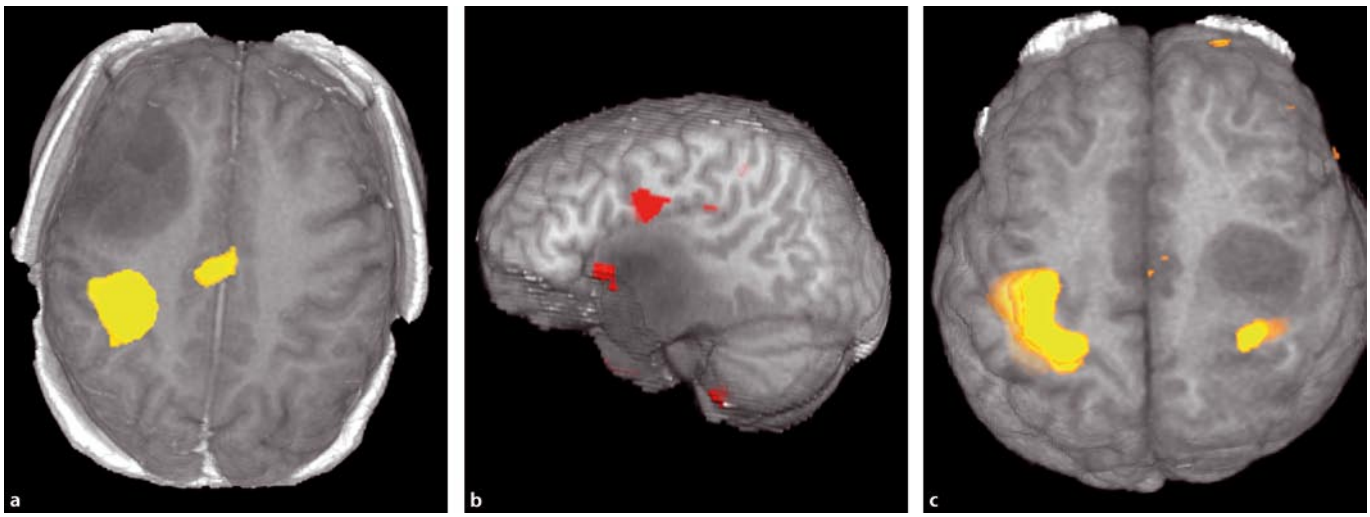

Fig. 1.17a–c fMRI maps imposed on 3D brain models. **a** Patient with a brain tumour of the right frontal lobe, **b** interrelation of Broca's area in patient with glioma of the left temporal lobe, **c** interrelation of motor centres in the case of bilateral stimulation in patient with astrocytoma of the left posterior frontal lobe

posed on T_1 MRI sequences (Fig. 1.16). Map construction methods (for instance, brain wave algorithms) subtract images obtained during neuron stimulation from control images obtained in the absence of stimulation. The subtracted image is imposed on a control scan according to its location, and areas of increased neuronal activity are marked with colour. The revealed functionally significant areas could be "imposed" on a T_1 MRI sequence of the same section or on a three-dimensional (3D) brain model, and thus it is possible to estimate the ratio between the affected area (tumour) and functionally active brain areas, for example, motor, sensory or visual cortex (Fig. 1.17).

1.5.1 Clinical Application of fMRI

Neuronal activity mapping enables planning the surgical approach and studying of the pathophysiological processes in brain. This method is used in neurosurgery in studying cognitive functions. Its perspective is in revealing the epileptic foci.

Currently, fMRI is an integral part of MRI protocol in patients with brain tumours located close to the functionally important brain areas. In the majority of cases, the examination results adequately reflect the location of sensomotor, speech and acoustical areas of brain cortex. However, according to

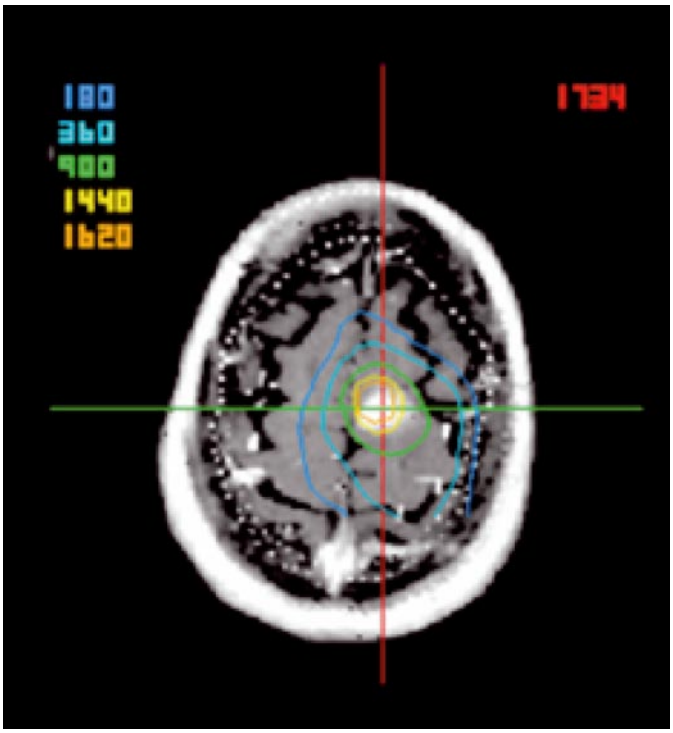

Fig. 1.18 The calculation of the radiation dose to brain tumour depending on location of functionally significant cortical areas

literature and our own study, 8–30% of all observation are not informative due to motion artefacts, lack of precise tests execution by the patients and damage to the above-mentioned cortical centres by tumours.

In cases in which fMRI can locate active cortical areas, in 87% of cases there is a correspondence with the results of intraoperational electrophysiological methods, within 1-cm limits, and in 13% of cases, within 2 cm. This is evidence of the high accuracy of the fMRI technique (Nennig et al. 2007).

Performing fMRI (currently it is conducted for somatosensory and visual cortices) and tractography with mapping of the functionally active cortical areas, pyramidal or optic tracts. Imposition of these maps over 3D brain images is promising within the framework of one MRI examination for patients with brain tumours. Based on these data, neurosurgeons plan the interventional approach and estimate the volume of neoplasm resection, and radiologists assess the areas of radiation and its distribution in tumour (Fig. 1.18).

1.6 Proton MR Spectroscopy

MR spectroscopy (MRS) is a non-invasive method of brain metabolism assessment. Proton (^{1}H) MRS is based on a "chemical shift"—the change of proton resonant frequency. This term was developed by N. Ràmsey in 1951, for defining a distinction between frequencies of separate spectral peaks. The chemical shift measured unit is in parts per million (ppm). Following are the main metabolites and corresponding values of the chemical shift; peaks of those metabolites are detected in vivo in the proton MR spectrum: *N*-acetylaspartate (NAA), 2 ppm; choline (Cho), 3.2 ppm; creatine (Cr), 3.03 and 3.94 ppm; *myo*-inositol (mI), 3.56 ppm; glutamate and glutamine (Glx), 2.1–2.5 ppm; lactate (Lac), 1.32 ppm; and a complex of lipids (Lip), 0.8–1.2 ppm.

The MR spectrum contains the extensive information about a substance. The peaks' positions determine a chemical composition, and their width reflects the T_2 relaxation time. The area under resonant peak is proportional to proton density and allows calculation of the metabolite concentration. Proton MRS has grown from the high-resolution nuclear MRS. In adjusting of the MR spectrum, the adjusting of MR scanner during examination (prescan) plays a significant role.

Currently in proton MRS, two basic methods are used, single voxel (SV) and multivoxel (MV, or chemical shift imaging). MRS is a single-stage detection of spectra from several brain areas. Multinuclear MRS, based on phosphorus, carbon and other element nuclei, are entering clinical practice (Rinck 2003).

In the case of SV-MRS, only one brain element (voxel) is chosen for the analysis. The metabolite's peak distribution on the chemical shift scale (in parts per million) is obtained based on analysis of the structure of frequencies in a signal registered from this voxel (Fig. 1.19). SV-MRS uses pulse sequences point-resolved spectroscopy (PRESS) or stimulated echo acquisition mode (STEAM). STEAM has higher resolution on frequency, but it is very sensitive to the patient's motions. Resolution of PRESS is a bit lower than is STEAM; however, it is less sensitive to motion. The ratio between metabolites peaks in a spectrum, decrease or increase of the height of separate peaks in a spectrum, are like fingerprints of brain biochemistry: on their basis, it is possible to make a non-invasive assessment of the biochemical process in tissues.

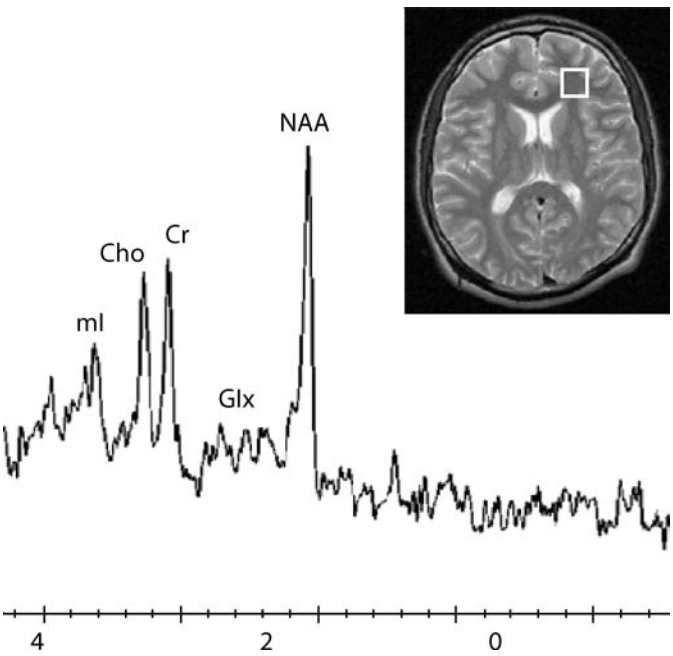

Fig. 1.19 Single-voxel proton MRS of brain tissue in a normal volunteer. The peaks of main metabolites are marked on the image

MV-MRS simultaneously obtains MR spectra for several voxels, and thus it is possible to compare spectra from different elements in an examination area (Fig. 1.20). Processing of the MV-MRS data enables construction of a parametrical map of brain. The concentration of particular metabolites on this map is marked by colour, and thus it is possible to visualise the metabolite distribution in brain, i.e. to obtain an image weighed on the chemical shift.

NAA is the most visible peak in the 1H spectrum (at 2 ppm). In reality, this peak includes different combinations of macromolecules with NAA: *N*-acetylaspartylglutamate, glycoproteins, and amino acid residues, and thus this peak could be more appropriately termed "*N*-acetyl groups". It is considered that in the adult brain, NAA plays at least two roles: (1) as a predecessor of brain lipids, and (2) as a participant in coenzyme A interactions.

Some researchers believe that NAA is metabolically inert, and it participates only in maintenance of "deficiency anion" balance in neutral tissues, so it is the indicator of processes with neurotransmitter–neuromodulator participation, and its basic function is to be the form of free storage of aspartate (Ureniak et al. 1992). In an adult brain, the concentration of NAA in the cortex is higher than in white matter, as the majority of NAA is located in neurons and their branches. Acetyl-CoA-L-aspartate-*N*-acetyltransferase is a synthetic enzyme used for obtaining NAA in mitochondria.

Acetoaspartase is an enzyme that decomposes NAA, and it is mainly located in astrocytes; thus, NAA decomposition occurs mainly in glial cells, and that explains the low NAA concentration in mature glia. Due to the mainly neuronal and axonal NAA location, the NAA peak decreases in cases of neurodegenerative diseases. Animal experiments have confirmed that decreased NAA correlate with neuronal necrosis. Absolute or relative (in relation to creatine) decrease of this peak is considered an indicator of neuronal and axonal damage.

However, as NAA is synthesised in mitochondria, theoretically, the exhaustion of energy without permanent neuronal damages could lead to temporal NAA decrease. In children, the NAA concentration in grey and white matter is identical. Rather high concentration of NAA in immature white matter is related with very high activity of lipid synthesis; research of immature brain demonstrated that oligodendroglia predeces-

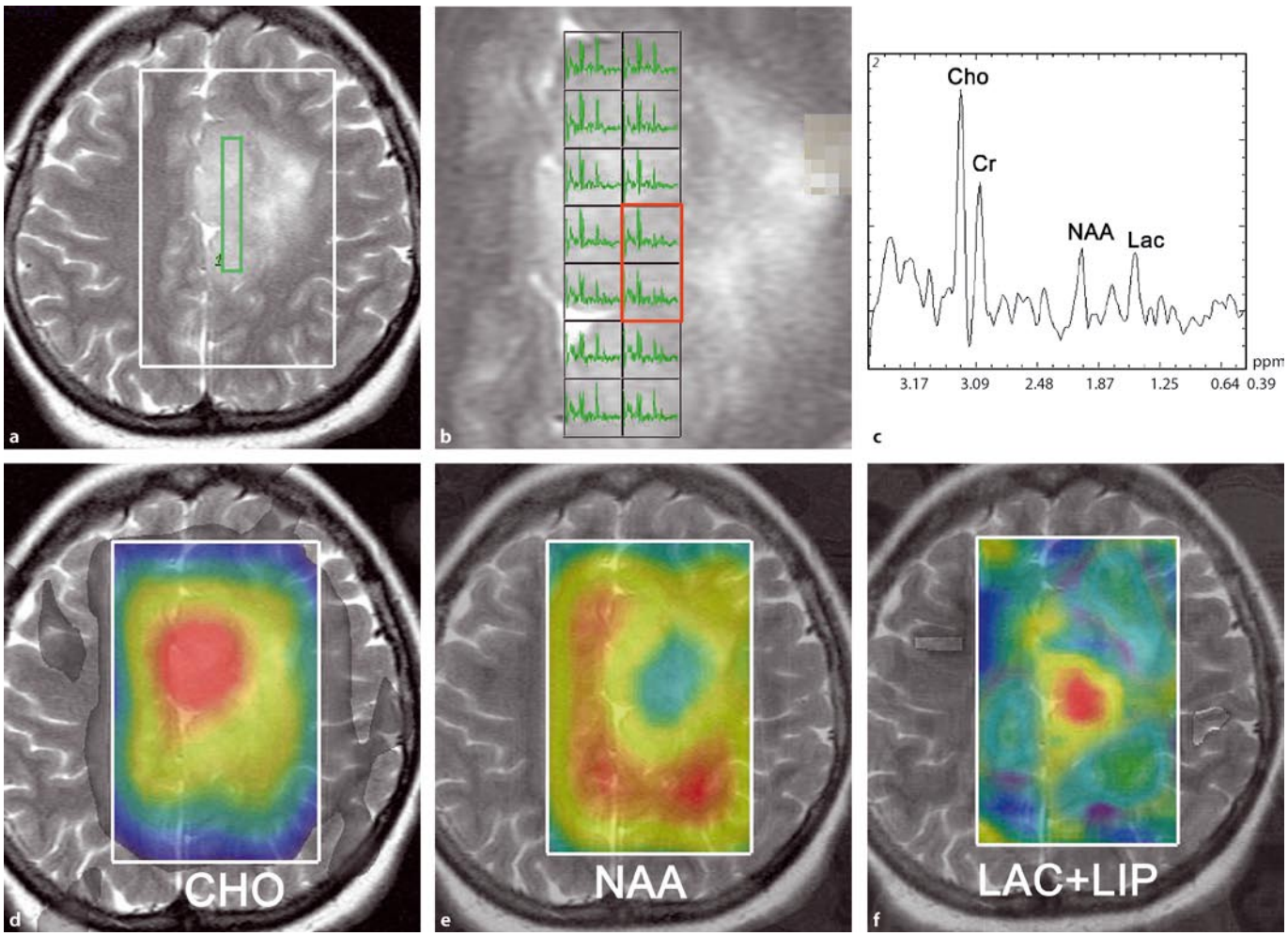

Fig. 1.20e–f Multivoxel proton MRS in a patient with a brain tumour. **a** Spectra presentation in each voxel; **b** enlarged image with measured points placement; **c** spectrum of tumour's tissue, with typical glioma metabolite changes; **d–f** colour map of different metabolite contents

sors have twice more NAA than do underdeveloped neurons.

The *choline* peak at 3.21 ppm contains the cumulative contribution of trimethylammonium protons (–N(CH3)3+) in choline, betaine and carnitine plus H5 protons of mI and taurine. The choline contribution is a sum of signals from several choline-containing chemical compounds (phosphoryl choline, glycerophosphoryl choline and free choline), and probably together with choline, which is present in a form of a polar head group in lipid membranes. MRS might not detect the compounds of choline embedded in a membrane; however, in the case of cell membrane destruction caused by the disease, choline is released, accumulated and may be detected. Choline is a structural component of cellular membranes, especially myelin membranes. The choline peak tends to increase in highly malignant tumours and neurodegenerative diseases. Focal inflammation, which leads to considerable local cellularity and often to significant cellular membranes damages, could also result in increasing of choline peak.

The *creatine* peak at 3.03 ppm is caused by protons of methyl (CH3) group of creatine, phosphocreatine, lysine and glutathione. It appears that phosphocreatine is the basic molecule for maintenance of energy-dependent systems in all brain cells. Its concentration is maximal in a cerebellum, followed by grey, and then by white, matter. Usually, it is assumed that the general creatine level is stable in different situations; therefore, the height of creatine peak is often used as reference in comparison with the height of other metabolites peaks.

MI that has two peaks at 3.56 and 4.06 ppm, and it is supposed it serves as storage of membranous phosphoinositides, which are the second messengers of the hormonal systems, and which participate in CNS enzyme regulation. It is one of major growth factors, and it is a predecessor of phosphatidylinositol, which in turn is a part of the lipid layers of cellular membranes. It is located primarily in glial cells and therefore could serve as a specific glial marker. Its other possible functions include osmoregulation, cellular nutrition and detoxication. The low combined peak at 3.56 ppm is from glycine and inositol-1-phosphate.

Scyllo-inositol is an isomer of mI, which is not exposed to metabolic changes that could inhibit transport and mI (embedding) association with lipids. The singlet peak at 3.35 ppm is believed to originate from the six protons of methane in a molecule of cyclic alcohol of *scyllo*-inositol, not from taurine as was thought previously. The singlet nature of resonance is caused by a chemical shift, and it is in agreement with biochemical concentration levels of mI compounds, and elimination of the other metabolites of 1H MRS spectra of mammalian brains in vivo as well as in vitro.

The presence of glucose in brain tissues can be detected with MRS, with short TE time by a singlet at 3.43 ppm. The area under this singlet can be used for calculation of brain glucose concentration.

It is possible to detect lactate, which is detected by its typical doublet located in 1H MRS spectra around 1.32 ppm, in trace quantities corresponding to terms of pregnancy. It is believed that lactate, if found in greater quantities, especially in the first hours of life, is an indicator of brain damage. However, lactate presence in 1H MRS is a normal finding in prematurely born children. The small peak present in the fetus decreases toward 40 weeks' gestation. Lactate concentration varies as the brain matures—in newborns, it is higher in less- matured areas of the brain, such as parietal, anterior frontal and temporal. In more mature brains, lactate concentration is higher in the basal ganglia and central gyri.

In a case when 1H MRS has a short TE, several small peaks appear in 1H MR spectra at 2.1 and 2.4 ppm, corresponding to the protons in *glutamine* and *glutamate*. Unfortunately, in the case of a magnetic field induction of 1.5 T (usually used in the clinical setting), these peaks overlap, and their separation is difficult on a background of NAA peak. In all probability, with the use of higher magnetic fields, these peaks could become distinguishable, and their analysis could help with detection of metabolic brain damage (which is accompanied by a change of the glutamate peak).

Currently, the following areas of proton MRS clinical application are being considered: injury, metabolic and mitochondrial damages, as well as inflammatory and volumetric disorders.

1.6.1 Brain Tumours

MRS is now widely used in an estimation of various volumetric brain formations (Meng 2004; Hourani 2006). In spite of the fact that according to MRS data, it is impossible to predict with sufficient confidence the neoplasm histological type, nevertheless, the majority of researchers agree that tumoural processes as a whole are characterised by a low NAA–Cr ratio, increase in Cho–Cr ration, and in some cases, by the lactate peak (Fig. 1.21).

In the majority of performed MRS examinations, proton spectroscopy is used in differential diagnostics of astrocytoma, ependymoma and primitive neuroepithelial tumors (PNET). It is noted that typical signs of astrocytoma and ependymoma are the decrease in the NAA–Cho ratio and increase in the ratio of Lac–Cho peaks in relation to those in a healthy hemisphere. In comparison with these tumours, PNET are characterised by an increase in the NAA–Cho ratio and a lower Lac–Cho ratio, which is related to a higher level of Cho in patients with PNET, as with malignant neoplasm.

For astrocytoma, in general, the increase of the Cho peak, the change of mI peak (depends on the malignancy level), the significant reduction of the NAA peak and the appearance of a Lac peak are typical. (In some cases, the combination of Lac and Lip peaks is observed, representing single Lac–Lip complex.)

For benign astrocytoma, the reduction of NAA peak is typical, and the increase of Cho peak is observed. The height of the mI peak can remain unchanged, or it can rise insignificantly in comparison with contralateral tissues not affected by tumours. The Lac peak is characterised by small elevation, and in rare cases, it cannot be detected at all (Fig. 1.21a).

The Cho and Lac peak rise, while the mI peak falls with the increase of malignancy level—in particular, in cases of anaplastic astrocytoma (Fig. 1.21b). The NAA peak is reduced in comparison with its height in the spectrum of benign astro-

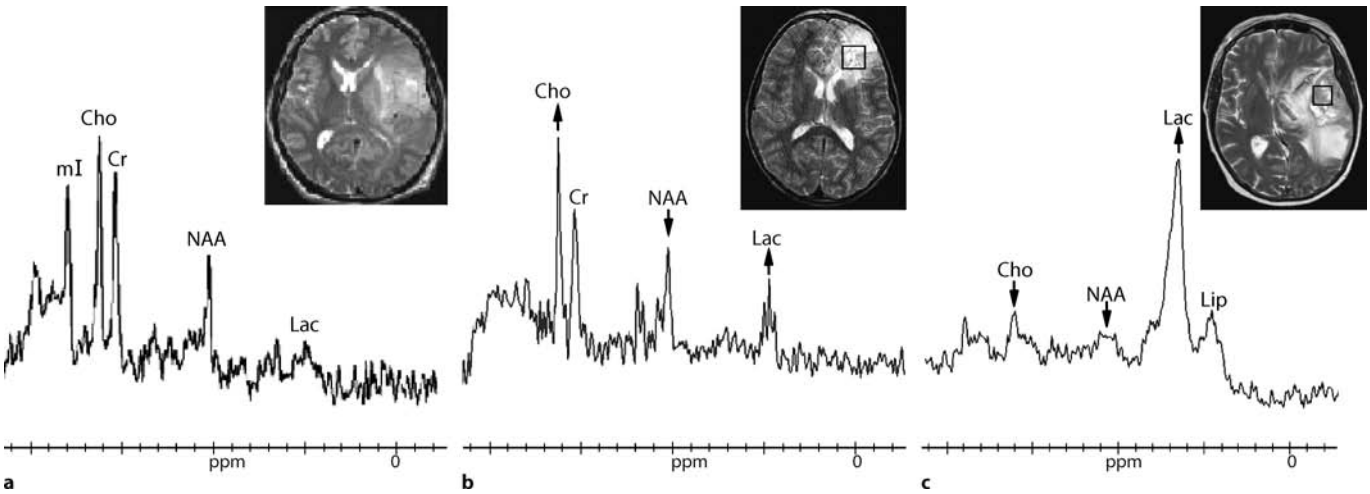

Fig. 1.21a–c T_2 MRI and proton MR spectra of gliomas with various malignancy levels. **a** Astrocytoma grade I–II, **b** anaplastic astrocytoma, **c** glioblastoma

cytoma. The marked or full reduction of NAA and mI peaks, and the sharp increase of the Lac peak, are observed in spectrum of glioblastoma, which is characterised by the presence of a necrosis area. At the same time, the Lip peak appears and overlaps the Lac peak, and visually, these peaks looks like single complex (Fig. 1.21c). Generally, the height of Cho peak is sharply increased.

In clinical practice, it is important to use MRS during postoperational period for diagnostics of the continued neoplasm growth, tumour relapse or radiation necrosis.

As a rule, treatment of brain tumours is a combination of surgery with chemo- and radiotherapy. However, current methods and doses of radiotherapy could cause the death of not only tumour cells, but also of healthy cells, especially in cases of lowered sensitivity threshold for radiotherapy. First, endothelium cells of vessels suffer, then brain oedema appears, and as a result, a zone of radiation necrosis could appear. According to statistics, in more than 5% of all patients who undergo radiotherapy because of a neoplasm, brain damage is diagnosed by the end of the first year near the tumour as well as in other areas.

The differential diagnosis between the continued growth, tumour relapse and radiation necrosis is extremely complicated, even with functional CT and MRI examinations. The tumour and radiation necrosis both have the similar CT and MRI pictures. CM accumulation in radiation necrosis is almost the same as in an area of tumour growth.

In such cases, ^{1}H MRS is a useful additional method in differential diagnostics. In a radiation necrosis spectrum, the so-called dead peak, a wide Lac–Lip complex in the range of 0.5–1.8 ppm on a background of a full reduction of other metabolites' peaks, is a typical attribute. In some cases, the Cho peak can be observed, which complicates the differential diagnostics of radiation necrosis and relapse of tumour with necrotic component (glioblastoma, metastasis).

The diagnosis of lymphomas is an important neuroradiology problem. Differential diagnostics of these tumours based on only routine CT and MRI is complicated, and combined chemo- and radiotherapy treatment is more preferable than surgical removal (Kornienko 2004). Therefore, the correct diagnosis influences the tactic choice in treatment and the prognosis of disease. In the majority of cases, it is necessary to differentiate lymphomas with glial tumours and metastasis. The common trend of changes in peaks of Cho, Lac and NAA is observed in lymphoma spectrum as well as in that of astrocytoma. However, these changes are different. With the lymphoma spectrum, the changes of peak heights are not so expressed. The Cho peak increases moderately, and the increased of peak of the Lac–Lip complex is substantial, whereas the decrease in the NAA peak is insignificant.

1.6.2 Ischaemic Stroke

Usually, clinical signs and the patient's medical history provide the physician enough information for establishing the correct diagnosis in an overwhelming majority of the cases. Nevertheless, in an outpatient practice, it is sometimes necessary to differentiate ischaemic lesion from primary brain tumours (low-malignant astrocytoma).

CM administration does not provide sufficient information since in an acute stroke phase, there is no brain–blood barrier damage, and CM might not accumulate in the affected area. The same is true of astrocytoma. Proton (^{1}H) MRS use in such cases facilitates considerably differential diagnostics and an establishment of final diagnosis (Podoprigora et al. 2003). In addition, ^{1}H MRS performed permits estimation of the efficiency of conservative treatment and prognosis.

In the first hours after an ischaemia onset, anaerobic glycolysis begins in the affected brain area, i.e. Lac appears and its

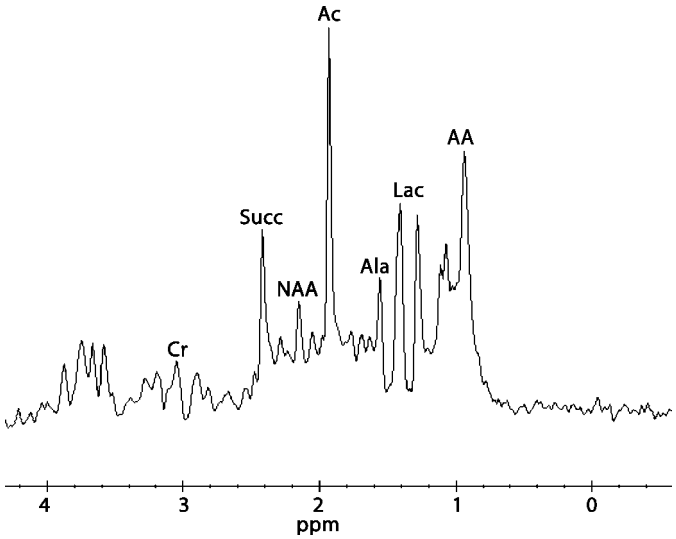

Fig. 1.22 Proton spectrum from the central area of abscess (peaks of metabolites revealed on the spectrum are marked)

level grows quickly, so the Lac peak is revealed in a spectra of acute and subacute ischaemic phases.

Hypoxia leads not only to neurons' dysfunction, but also to their death, which results in the decrease of neuronal mass in affected area. In the spectrum, it is reflected in the form of moderate reduction of the NAA peak. The behaviour of the Cho peak in the case of ischaemia is not so clear. Its decrease is observed in the majority of cases, but this peak increases in others. Possibly, in phases of acute and subacute ischaemia, the Cho peak increase could be related to damage of the integrity of myelin fibre membranes and release of metabolites. At later stages, the Cho concentration decreases, possibly caused by reduction of cell numbers due to their destruction, and accordingly, due to the reduction of total mass of cellular membranes containing Cho.

The restoration of the main metabolite peak heights toward normal values in repeated examinations (dynamic observation) is a favourable prognostic sign. The main metabolites' continued peak reduction combined with the appearance of the Lac peak indicates cell death in the ischaemic area.

Another aspect of the use of MRS is differentiation of the primary and secondary lesions revealed in the initial infectious and demyelination processes. Results of infection diagnostics are the most indicative (Pronin et al. 2002). In an abscess spectrum, there is a peak of the Lip–Lac complex as well as peaks specific for abscess content, such as acetate and succinate (the products of anaerobic glycolysis of bacteria), and amino acids valine and leucine (proteolysis products) on a background of absent core metabolite peaks (Fig. 1.22).

1.6.3 Epilepsy

Diagnosis of epilepsy includes numerous methods and examinations, and MRI is only one of them. At the same time, today MRI is the sole method that characterises anatomic changes in a targeted brain area, for example, in the case of medial temporal sclerosis or cortical dysplasia. MRS in such cases is an additional method of brain dysfunction detection since it reveals a decrease in the NAA peak and NAA–Cr ratio in the hippocampus and in an area of dysplastic changes in brain tissue.

1.6.4 Metabolic Disorders

MRS is an informative method for estimation of metabolic damages and primitive lesions of white matter in children. Although MRS is not very specific in case of leukodystrophic and metabolic CNS damage, its results nevertheless narrow the pool of possible brain tissue diseases. The majority of the above-mentioned forms of brain damage lead to NAA peak decrease due to neuronal–axonal degeneration and brain tissue loss (Fig. 1.23). In the case of methochromatic leukodystrophy, MRS reveals the significant decrease of the NAA

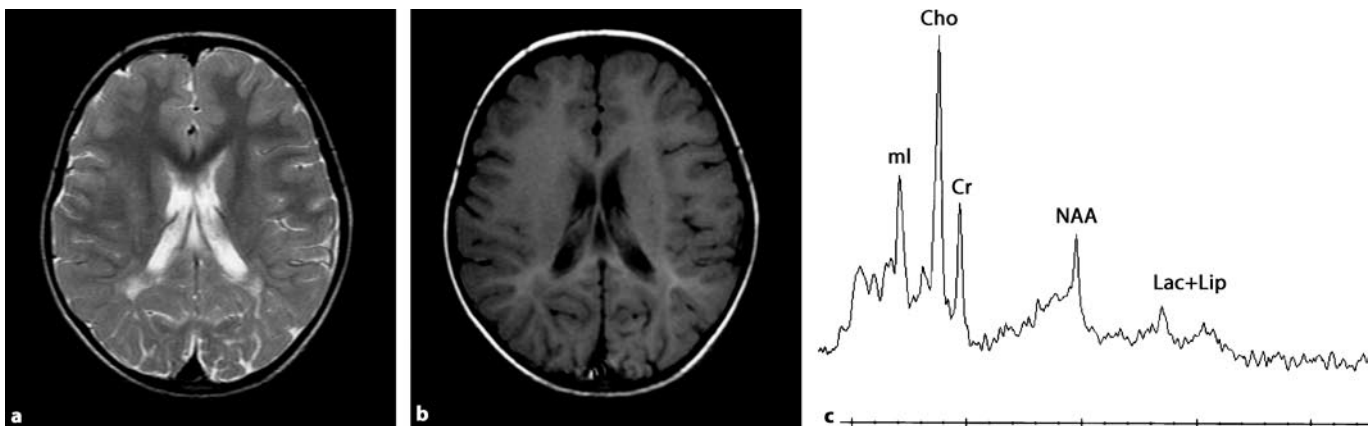

Fig. 1.23a–c Leukodystrophy in a 6-year-old child. MRI in T_2 (**a**) and T_1 (**b**) reveals areas of pathological hyperintense MR signal of uneven form behind the posterior horns of the left ventricles. MR spectrum from the pathological area demonstrates the decrease of the NAA peak and the increase of Cho and mI peaks (**c**)

peak and moderate increase of the Lac peak. A decrease of the Glx peak and an increase of the mI peak are observed.

In the case of Canavan's disease, MRS detects increase of the ratio of NAA–Cho and NAA–Cr peaks. MRS is a useful method of the brain condition estimation in patients with adrenoleukodystrophy. In this case, MRS detects the marked decrease of NAA–Cr and NAA–Cho peak ratios, the increase of Cho–creatine ratio, and the rise of Glx, mI and Lip peaks in an area of maximal changes, revealed with the help of standard MRI. The MR spectral changes in several types of hyperglycaemia including with the increase of glutamine peak (3.55 ppm) are relatively specific.

1.7 Phosphorus MR Spectroscopy

Phosphorus (^{31}P) MRS, which utilises resonant frequencies of phosphorus ^{31}P nucleus in various chemical compounds, is often performed on modern high-field MR scanners. The resonant frequency of ^{31}P is approximately 0.405 from resonant frequency of a hydrogen atom nucleus in water molecule. The main metabolites of phosphorus spectrum are: phosphomonoesters (PME); inorganic phosphate (Pi); phosphodiesters (PDE); phosphocreatine (PCr); and adenosine triphosphate (ATP), which has three peaks, α, β and γ, as each ATP molecule contains chemically variously three atoms of phosphorus. In Fig. 1.24, the phosphoric brain spectra of an adult with a normal brain (Fig. 1.24a) and patient with astrocytoma (Fig. 1.24b,c) are presented. In the normal brain, the highest central peak in a phosphoric spectrum is phosphocreatine (2.1 ppm).

The PDE peak is the second highest, and it reflects the presence of lipid predecessors like phosphoryl Cho, phosphoryl ethanolamine and Lip. This peak is located to the left of the PCr peak, and then the Pi and PME peaks follow. The PME peak includes MR signals from phosphates of sugars: glucose-6-phosphate, sucrose-6–phosphate, and hexose-6-phosphate, which partially overlap. To the right of the PCr peak there are three ATP peaks (γ, α and β). PCr and ATP play important roles in brain tissue energy metabolism. Phosphorus spectra are quantitatively estimated according to the ratio of metabolite peak heights to αATP peak height.

The homeostasis abnormality accompanied by the decrease of PCr and PDE peaks and increase of ATP peak is typical for tumour tissue (Maintz et al. 2002; Karsmar et al. 1991). Phosphoric spectra in patients with astrocytoma demonstrate visible decrease of PDE–αATP ratio in relation to normal spectra (Fig. 1.24). A meningioma phosphoric spectrum is often characterised by decrease of PCr–αATP and PDE–αATP (Maintz et al. 2002). A lymphoma spectrum shows substantial increase of the RME–αATP ratio (Karsmar et al. 1991). According to some authors, radio- and chemotherapy leads to gradual restoration of the height of phosphoric spectrum peaks (Maintz et al. 2002; Karsmar et al. 1991), but this report requires additional investigations.

Chemical shift between Pi and αATP peaks is used for the estimation of intercellular liquid acidity (pH), and the shift between Pi and PCr peaks for pH estimation in tumour tissue (Karsmar et al. 1991). According to Maintz et al. (2002), pH in brain tissue of an adult normally is 7.04 ± 0.01; in tumour tissue pH increases to 7.12 ± 0.02 in glioblastoma and to 7.16 ± 0.03 in meningioma.

Changes of metabolite peak heights of the phosphoric spectrum are observed during brain development in children within first the 3 years of life (van der Knaap et al. 1990), in cases of degenerate diseases (van der Knaap et al. 1991), hydrocephaly (Braun et al. 1999), ataxia (Bluml et al. 2003) and creatinine deficiency syndrome (Bianchi et al. 2007).

MR scanner adjustment (prescan) is often done manually, and ^{31}P MRS examination takes a long time. However, current work on the use of echo-planar pulse sequences for fast brain mapping based on ^{31}P MRS is being done (Ulrich et al. 2007). Fast mapping methods of products of phosphorus metabolism open the opportunities of visualisation of bioenergy changes during brain simulation, for example, the block stimulation in fMRI.

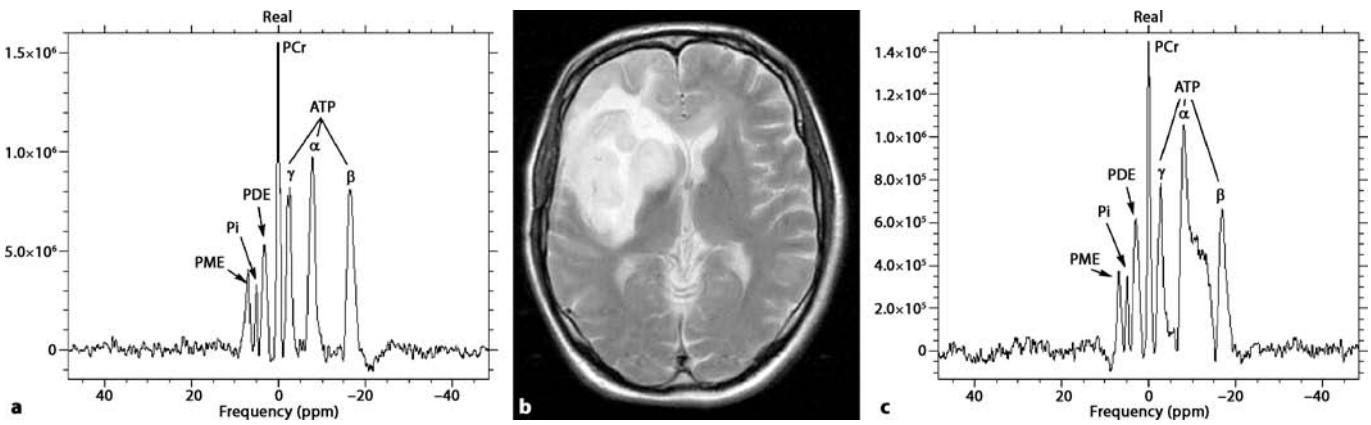

Fig. 1.24a–c Phosphorus MR spectra obtained in the magnetic field of 1.5 T. **a** ^{31}P spectrum of a normal adult brain. The main metabolites of the phosphorus spectrum are: phosphomonoesters (*PME*); inorganic phosphate (*Pi*) phosphodiesters (*PDE*); phosphocreatine (*PCr*); and adenosine triphosphate (*ATP*), which has three peaks, α, β and γ. **b** T_2-weighted image of a tumour. **c** ^{31}P spectrum of a patient with anaplastic astrocytoma, demonstrating the decrease of PDE–αATP peaks ratio

1.8 Neuroradiology and Information Technologies

As the volume of diagnostic information grows, network support and the use of specialised workstations for the expanded digital processing of examination data is becoming increasingly more necessary. Workstations and digital diagnostic devices use the same user interfaces, browser program for examination results, programs of CT and MRI data processing, and they are equipped with the programs for recording images on CD and other magnetic carriers which assures that the multimodal operations function well.

The use of digital technologies in modern radiology is the standard for all developed countries, and it is taking root in Russia. The old film technologies of data presentation and storage of films are gradually become obsolete. The need for additional computer processing for obtaining more detailed information on the pathology in question is arising more often (Rodionov et al. 2002).

Modern superfast spiral CT scanners and high-field MR scanners are constructed with the use of the newest technical achievements, modern hardware and the software. In diagnostically complex cases, after CT and MRI imaging, the neuroradiologist can continue to study the obtained data for making a diagnostic conclusion without the patient present. For this purpose, the diagnostic images can be digitally stored and transferred to a graphic computer station for the subsequent processing and analysis by a local network or by the Internet.

Modern diagnostics requires additional postprocessing on special graphic computer stations equipped with powerful software packages with mathematical analysis and modelling, which can be performed, again, in the absence of the patient. Use of remote graphic stations for postprocessing is prompted by the necessity of 3D image construction, including the combined models of soft tissues of a head, skull, brain and its vascular system for neurosurgery intervention modelling (Fig. 1.25).

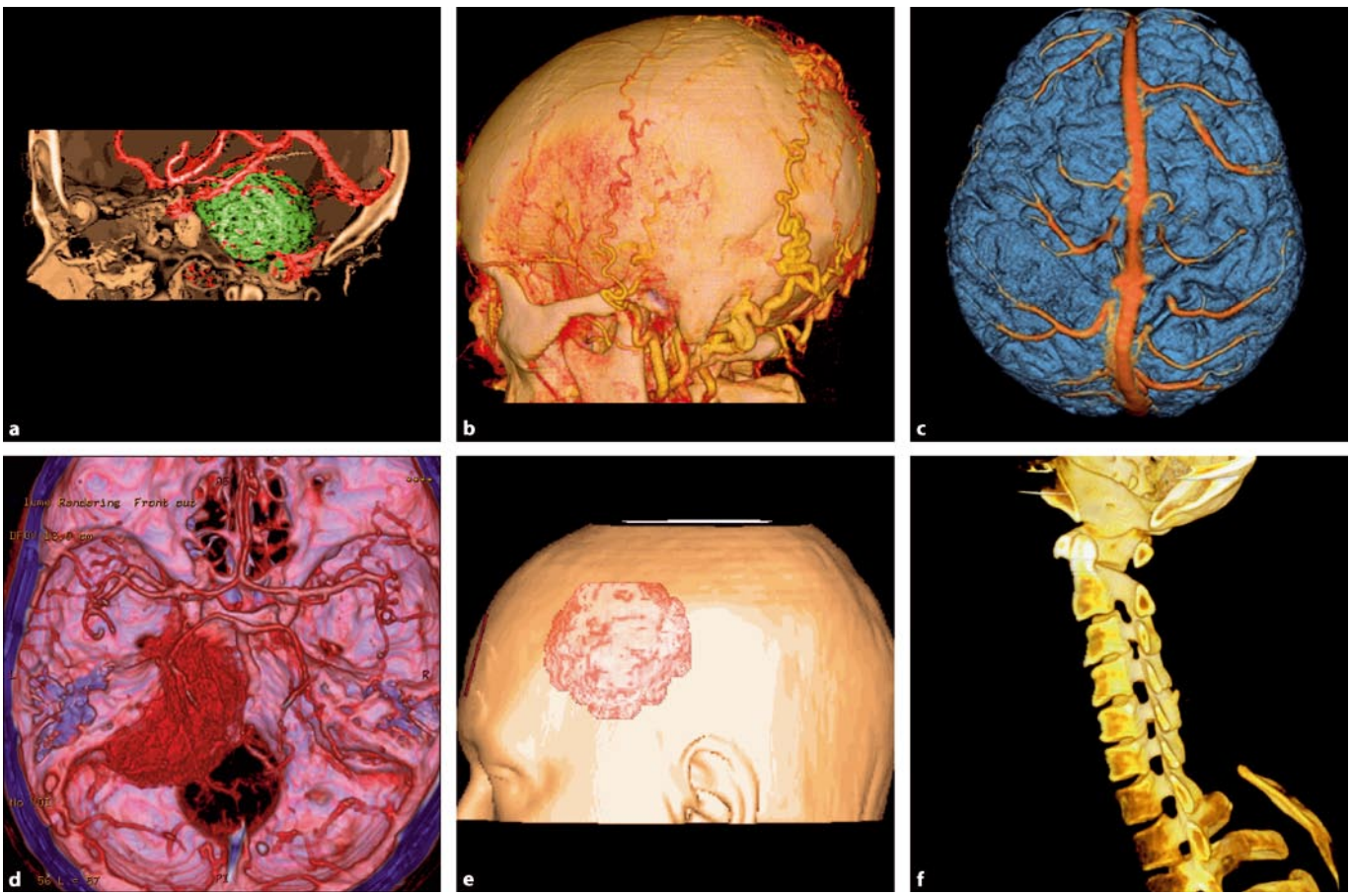

Fig. 1.25a–i 3D modelling based on CT and MRI for planning of neurosurgical intervention. **a** 3D superposition of 3D models of bones, brain vascular structures and tumour, with the use of CT (meningioma of posterior cranial fossa), **b** dural arteriovenous fistula of parietal region (CT angiography), **c** superposition of cortical surface and convex vein (based on MRI), **d** 3D superposition of bones, brain vascular structures and tumour (CT angiography, volume rendering, petroclival meningioma), **e** 3D superposition of 3D models of the skin surface and tumour (falx meningioma), **f** 3D model of cervical part of vertebra (view from the internal surface of vertebral canal to the intervertebral foramens in the case of a removed section of vertebra in patient with spondylosis and intervertebral foramen compression at the C3–C4 level), **g–i** *see next page*

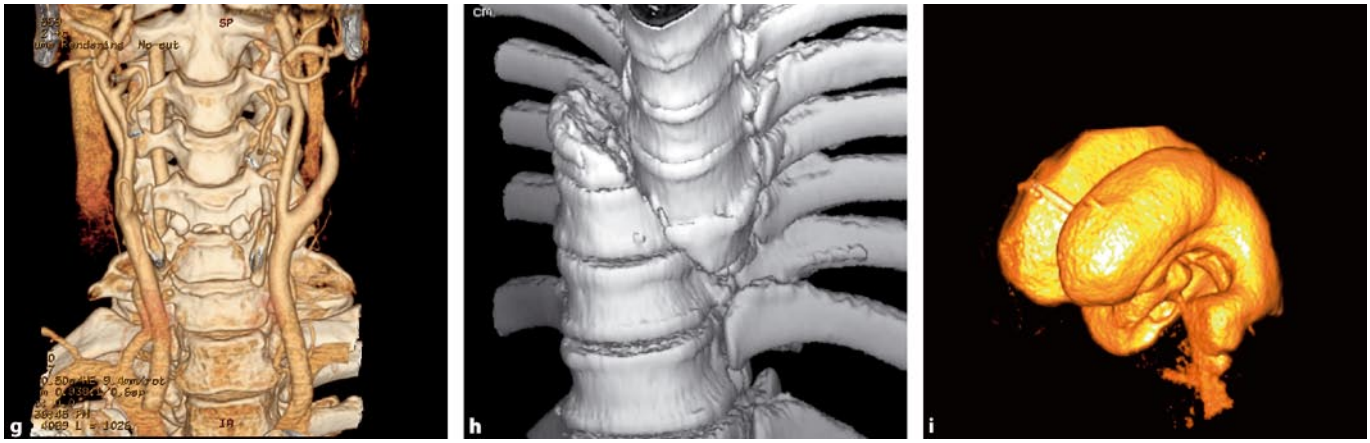

Fig. 1.25a–i (*continued*) 3D modelling based on CT and MRI for planning of neurosurgical intervention. **g** 3D processing of volume-rendered data of CT angiography of cervical vessels, **h** 3D processing of CT data in patient with a fracture of a thoracic vertebra with dislocation, **i** 3D model of ventricular system in child with open hydrocephalus

The analysis of DTI (calculation of average and anisotropic diffusion speed, construction of parametrical maps of fibre tracing, and so forth), perfusion examinations (calculation of blood flow parameters, parametrical maps construction), and other such parameters, requires mathematical processing. As a rule, subsequent viewing of the obtained results, for example, in clinical conferences or directly in operation room of a surgical hospital, is also carried out on the graphic stations.

The special unified data format Digital Imaging and Communications in Medicine (DICOM 3.0) developed by the American College of Radiology (ARC) and National Electrical Manufacturers Association (NEMA) is used for storage and transfer of medical images in modern radiology. In modern medical clinics, imaging results are often stored on a short-term basis in the operative memory of the diagnostic device (CT, MRI, angiosystem) or in the operative memory of a graphic station. However, operative memory is limited and is not intended for the long-term data storage necessary in scientific work.

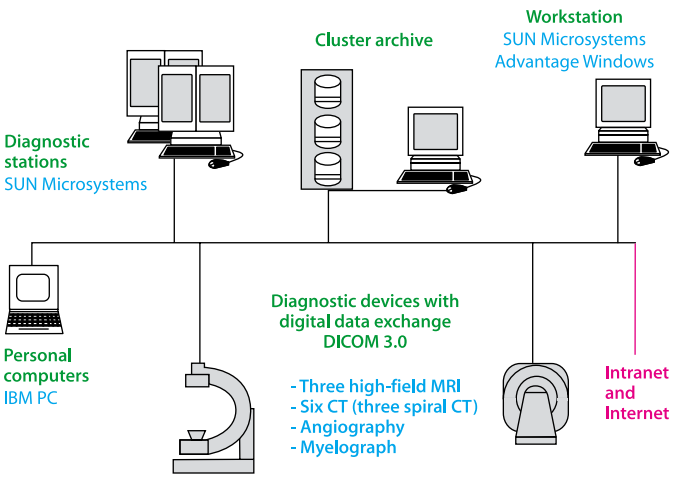

Fig. 1.26 Schema of the computer radiological network for obtaining, storage, transmission and postprocessing of medical images in the Neuroradiology Department of Burdenko Institute of Neurosurgery

As a rule, the archiving of examination results is necessary for long-term storage on any replaceable data carriers (for example, magneto-optical discs). Another variant is the use of Picture Archiving and Communication System (PACS), which requires the creation of special remote archives on servers in which rather large files can be stored for a long time in a "hot" state, and in this case, the interesting information is quickly accessible via network for search and viewing, and if necessary, for new data processing.

The digital storage of medical data is more preferably in comparison with film archives. Films could be stored for about 10 years in cases of strict compliance with all storage rules, while digital archives could exist indefinitely. Images are accessible for repeated calculations and analysis, which is especially important in neuroradiology, due to frequent necessity of dynamic observation for the patient during long periods. Taking into account the high cost of film and significant expenses for service of photographic developing apparatus, it is no surprise that digital technologies of storage, transfer and representation of the medical information are increasingly coming into practice all over the world.

The Neuroradiology Department of the Burdenko Neurosurgical Institute of Russian Academy of Medical Science developed a system to organise the information radiological system for obtaining, storage, transfer and postprocessing of diagnostic medical images. This system covers all diagnostic devices in the Neuroradiology Department. Moreover, it includes several graphic stations for viewing and postprocessing of medical images. The rooms equipped with digital diagnostic devices, and working and viewing graphic stations, have special connections to the network printers for image printing to film. Personal computers of scientific employees—engineers

Fig. 1.27 Operating room with a navigational system for surgery

and researchers—located in the rooms of the Neuroradiology Department are connected to the network and equipped with the special software capable of working with DICOM images (Fig. 1.26). It is necessary to note that, for the past 10 years, the quantity amount of diagnostic examinations performed with use of digital methods has grown significantly, and image processing has become more complicated.

1.9 Navigation in Neurosurgery

Development of digital medical technologies, appearance of fast portable computers and successes in neuroradiology due to the advent of CTI and MRI paved the way for celebrated technological breakthroughs in stereotactic neurosurgery. This has led to development of modern navigating systems that enable surgeons to navigate quickly and precisely in the 3D space of a surgical incision during operation, with a 1- to 2-mm precision. Such systems allow surgeons to perform intervention with minimal injury to the surrounding tissues.

Such systems use so-called frameless technology, unlike classical stereotaxis, which uses a frame-based navigating method. Navigation is based on "binding" of space coordinates to certain reference points that have static positions in geonavigating systems, e.g. stars or geodetic towers. Classical medical stereotactic devices use for these purposes a special frame fastened tightly to a patient's skull before the operation. All further calculations are based on the mutual relation between intracranial structures and the reference points of a frame and its geometrical centre. Navigation of the surgical tool is made with the help of relatively large facilities such as various arches and guides fastened to a frame. Such technical decisions in classical stereotaxis limits the neurosurgeon's actions in an incision and allows the carrying out of only simple manipulations (biopsy, implantation of electrode, catheter, cyst lancing).

The essence of frameless navigation is the following: Based on MRI and CT data, obtained before operation (as a rule, for 1–2 days), 3D images of the patient's head are built with graphic station software. The surgeon, according to the 3D image, chooses accessible reference points (for example, a tip of a nose, teeth, curves of an auricle) on a surface of the patient's head.

Before the operation and after introduction of narcosis, the special small navigating frame [with a light-emitting diode (LED)], which, unlike classical stereotaxis, can be fixed practically any place on the head and in any way suitable for the given operation, is firmly fastened to the patient's head at some distance from that area of interest. This frame, in the form of a partial arch, does not close the operational field and does not limit the surgeon in his or her actions. With the use of a special LED pointer, a preliminary "registration" is performed, i.e. the computer system "fuses" a 3D image of the patient's head from its memory with real head position. All systems consist of the aerial receiver, LED pointer, reference arch and computer algorithm of work with the 3D image. This allows the neurosurgeon at any moment of operation to determine the position of his or her tool, with 1- to 2-mm precision, to plan an access trajectory, and to move toward the chosen target with the optimal and least invasive way (Fig. 1.27). Today, the optimal application for frameless navigation is the surgery of basal and small convex located tumours (Fig. 1.28) and for removal of foreign bodies from the skull cavity. Methods of combining CT, MRI and angiographic data into 3D models of the head (fusion algorithm) is especially advantageous in radiosurgery, allowing minimisation of pathological areas, with a 0.1-mm precision during the targeting of radiation to brain tissues (Fig. 1.29).

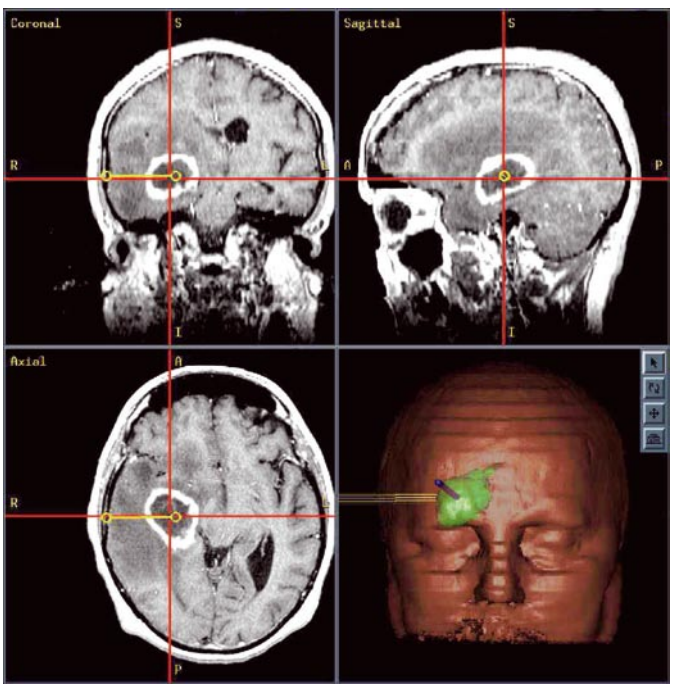

Fig. 1.28 Monitor of a workstation during preparation of removal of a brain tumour

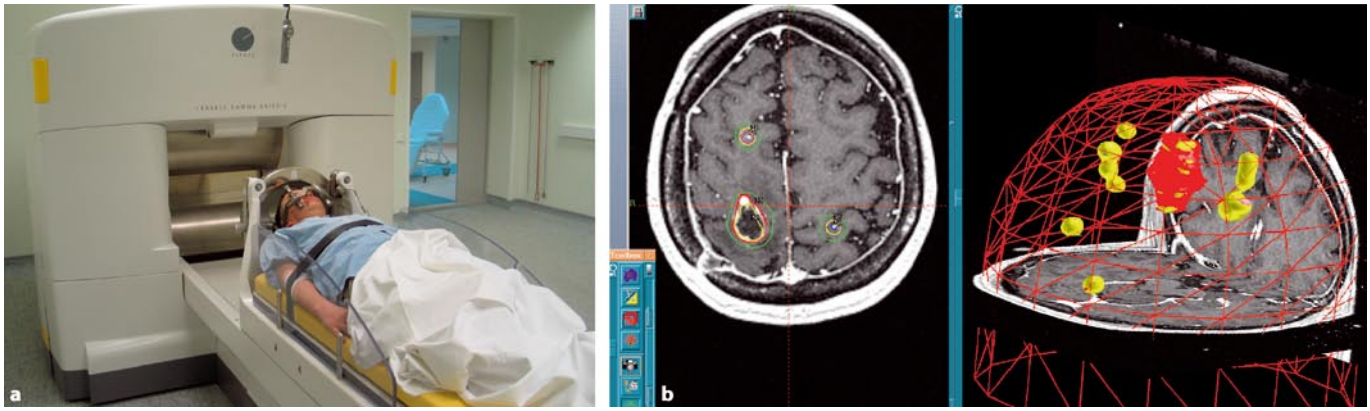

Fig. 1.29a,b Radiosurgical equipment. **a** Gamma knife device in the Burdenko Institute of Neurosurgery, **b** schema of target calculation (in the planning stage) according to CT and MRI data

References

1. Alsop D, Detre J (1996) Reduced transit time sensitivity in non-invasive magnetic resonance imaging of human cerebral blood flow. J Cereb Blood Metab 16:1236–1249
2. Aroutiunov A, Kornienko V (1971) Total cerebral angiography. Medicine Publishers, Moscow, p 167 (in Russian)
3. Batchelor P et al (2006) Quantification of the shape of fibre tracts. Magn Reson Med 55:896–903
4. Bianchi M et al (2007) Treatment monitoring of brain creatine deficiency syndromes: a ^{1}H- and ^{31}P MR spectroscopy study. AJNR Am J Neuroradiol 28:548–554
5. Bluml S et al (2003) Membrane phospholipids and high-energy metabolites in childhood ataxia with CNS hypomyelination. Neurology 61:648–654
6. Braun K et al (1999) Cerebral metabolism in experimental hydrocephalus: an in vivo ^{1}H and ^{31}P magnetic resonance spectroscopy study. J Neurosurg 91:660668
7. Cha S (2006) Update on brain tumour imaging: from anatomy to physiology. AJNR Am J Neuroradiol 27:475–487
8. Cha S et al (2007) Differentiation of glioblastoma multiforme and single brain metastasis by peak height and percentage of signal intensity recovery derived from dynamic susceptibility-weighted contrast-enhanced perfusion MR imaging. AJNR Am J Neuroradiol 28:1078–1084
9. Chai J-W et al (2007) Characterisation of focal brain lesions by gradient-echo arterial spine-tagging perfusion imaging. Neuroradiol J 20:149–158
10. Chepuri N, Yen Yi-Fen, Burdette J (2002) Diffusion anisotropy in the corpus callosum. AJNR Am J Neuroradiol 3:803–808
11. Feoktistov V (1938) The theory of tomography. Vestn Roentgenol Radiol 21:143–152 (in Russian)
12. Hesseltine S et al (2007) Application of diffusion tensor imaging and fibre tractography. Appl Radiol 1:8–23
13. Holshouser B et al (2006) Prospective longitudinal proton magnetic resonance spectroscopic imaging in adult traumatic brain injury. J Magn Reson Imaging 24:33–40
14. Hourani R et al (2006) Proton magnetic resonance spectroscopic imaging to differentiate between non-neoplastic lesions and brain tumours in children. J Magn Reson Imaging 23:99–107
15. Karsmar G et al (1991) P-31 spectroscopy study of response of superficial human tumors to therapy. Radiology 179:149–153
16. Knaap M van der et al (1990) Age-dependent changes in localised proton and phosphorus MR spectroscopy of the brain. Radiology 176:509–515
17. Knaap M van der et al (1992) ^{1}H and ^{31}P magnetic resonance spectroscopy of the brain in degenerative cerebral disorders. Ann Neurol 31:202–211
18. Konovalov A, Kornienko V (1985) Computed tomography in neurosurgical clinic. Moscow Medicine Publishers, Moscow, p 290 (in Russian)
19. Konovalov A, Kornienko V, Ozerova V, Pronin I (2001) Neuroimaging in paediatrics. Antidor, Moscow. p 435 (in Russian)
20. Konovalov A, Kornienko V, Pronin I (1997) Magnetic resonance imaging in neurosurgery. Vidar, Moscow, p 427 (in Russian)
21. Kornienko V, Pronin I, Fadeeva L et al (2000) Diffusion weighted imaging in study of brain tumours and peritumoural edema. J Vopr Neurochir 3:4–17 (in Russian)
22. Kornienko V, Pronin I, Golanov A et al (2004) Neuroimaging of primary lymphomas of brain. J Med. Visualis 1:6–15 (in Russian)
23. Kornienko V, Pronin I, Pyanykh O et al (2007) Study of brain perfusion, using CT. J Med. Visualis 2:70–81.
24. Le Bihan D, Breton E (1985) Imagerie de diffusion invivo par resonance magnetique nucleaire. CR Acad Sc II Paris 301:1109–1112
25. Le Bihan D, Turner R (1991) Intravoxel incoherent motion imaging using spin echoes. Magn Reson Med 19:221–227
26. Le Bihan D, P van Zijl (2002) From the diffusion coefficient to the diffusion tensor. NMR Biomed 15:431–434
27. Lee S-K et al (2005) Diffusion-tensor MR imaging and fibre tractography: a new method of describing aberrant fibre connection in developmental CNS anomalies. Radiographics 25:53–68

28. Leemans A et al (2006) Multiscaled white matter fibre track coregistration: a feature-based approach to align diffusion tensor data. Magn Reson Med, 55:1414–1423
29. Maintz D et al (2002) Phosphorus-31 MR spectroscopy of normal adult human brain and brain tumours. NMR Biomed 15:18–27
30. Meng L (2004) MR spectroscopy of brain tumours. Magn Reson Imaging 15:291–313
31. Mori S, van Zijl P (2002) Fibre tracking: principles and strategies. NMR Biomed 15:468–480
32. Moseley M, Butts K, Yenary M et al (1995) Clinical aspects of DWI. NMR Biomed 8:387–396
33. Mulkern R, Gudbjartsson H, Westin C et al (1999) Multicomponent apparent diffusion coefficients in human brain. NMR Biomed 12:51–62
34. Nennig E et al (2007) Functional magnetic resonance imaging for cranial neuronavigation: methods for automated and standardised data processing and management. Neuroradiol J 20:159–158
35. O'Donnell L-J et al (2006) A method for clustering white matter fiber tracts. Neuroradiol J 27:1032–1036
36. Pierpaoli C, Jezzard P, Basser PJ et al (1996) Diffusion tensor MR imaging of the human brain. Radiology 201:637–648
37. Podoprigora A, Pronin I, Fadeeva L et al (2003) Proton MR spectroscopy in ischaemic brain disease. ZH Neurol Psikhiatr SS Korsakova 9(Suppl.):162 (in Russian)
38. Pouratian N, Sheth S, Bookheimer S et al (2003) Applications and limitations of perfusion-dependent functional brain mapping for neurosurgical guidance. Neurosurg Focus 15:1
39. Pronin I, Kornienko V, Podoprigora A et al (2002) Complex MR imaging of brain abscesses. J Vopr Neurochir 1:7–11 (in Russian)
40. Ramsey N, Hoogduin H, Jansma J (2002) Functional MRI experiments: acquisition, analysis, and interpretation of data. Eur Neuropsychopharmacol 12:517–526
41. Rinck P (2003) Magnetic resonance in medicine. The basic textbook of the European Magnetic Resonance Forum. Blackwell, London, p 246
42. Rodionov P, Serkov S, Fadeeva L (2002) Modern software in practice of functional diagnosis specialist. PC Mag 4:134–137 (in Russian)
43. Sen P-N, Basser P-J (2005) A model for diffusion in white matter in the brain. Biophys J 89:2927–2938
44. Serbinenko F (1974) Balloon catheterisation and occlusion of major cerebral vessels. J Neurosurgery 41:125–145
45. Sorensen A, Reimer P (2000) Cerebral perfusion imaging: principles and current applications. Thieme, Stuttgart, p 152
46. Stadlbauer A et al (2007) Changes in fibre integrity, diffusivity, and metabolism of the pyramidal tract adjacent to gliomas: a quantitative diffusion tensor fibre tracking and MR spectroscopic imaging study. AJNR Am J Neuroradiol 28:462–469
47. Sunaert S (2006) Presurgical planning for tumour resectioning. J Magn Reson Imaging 23:887–905
48. Tanner J (1970) Use of stimulated echo in NMR diffusion studies. J Chem Phys 52:2523–2526
49. Ting-Yim L (2002) Functional CT: physiological models. Trends Biotechnol 20:1–8
50. Ulrich M et al (2007) ^{31}P-^{1}H echo planar spectroscopic imaging of human brain in vivo. Magn Reson Med 57:784–790
51. Ureniak J et al (1992) Specific expression of *N*-acetylaspartate in neurons, oligodendrocyte type-2 astrocyte progenitors, and immature oligodendrocytes in vitro. J Neurochem 59:55–61
52. Waaijer A et al (2007) Reproducibility of quantitative CNS brain perfusion measurements in patients with symptomatic unilateral carotid artery stenosis. AJNR Am J Neuroradiol 28:927–932
53. Zavoisky EK (1945) Spin-magnetic resonance in paramagnetics. J Phys Acad Sci USSR 9:211–245 (in Russian)